Nonuniform superconducting states from Majorana flat bands

Sushanth Varada,* Aksel Kobiałka, Ankita Bhattacharya, Patric Holmvall, and Annica M. Black-Schaffer
Department of Physics and Astronomy, Uppsala University, Box 524, S-751 20 Uppsala, Sweden

(Received 11 May 2026; revised 17 September 2026; accepted 29 October 2026; published 17 November 2026)

Zero-energy flat bands within the superconducting gap can give rise to competing ordered phases. We investigate such phases in topological superconductors based on the magnetic adatom platform hosting a flat band of Majorana edge states. Our self-consistent calculations of the superconducting order parameter show the emergence of both a pair density wave with edge-localized amplitude modulations, often a bond-wave order, and a phase crystal characterized by longer-wavelength edge-localized phase modulations. Both these states lower the free energy by gapping out the Majorana flat band but use different mechanisms tied to the underlying topology. In fact, at zero temperature, the uniform superconducting solution with Majorana flat band never survives. Instead, a pair density wave appears when sufficient Majorana modes exist with oppositely signed topological winding numbers, while a phase crystal appears in regions of the phase diagram where one nontrivial winding number is heavily dominating. A crossover region connects these two states with modulations in both amplitude and phase. At finite temperatures, the pair density wave survives up to around 80% of the bulk superconducting transition temperature, while the phase crystal only appears at lower temperatures and the crossover region is also strongly suppressed. Our findings establish the ubiquity of emergent nonuniform superconducting phases and their temperature-dependent behavior in topological superconductors.

DOI: 10.1103/q8w8-y7fk

I. INTRODUCTION

Nonuniform superconducting ground states provide a fascinating platform to study the interplay between spontaneous symmetry breaking and ordered states [1–8]. Flat bands of zero-energy states within a superconductor can easily become thermodynamically unstable to interactions due to their extensive ground-state degeneracy, facilitating a competition between different symmetry-breaking instabilities [9]. This has been extensively studied at the (110) surface of d-wave superconductors, especially in the context of cuprate high-temperature superconductors [9–27]. Notably, different superconducting states can occur that lower the free energy by shifting the zero-energy flat bands to finite energies, including a subdominant superconducting order [11–15,28,29], spontaneous but translationally invariant supercurrents [16,30–34], and edge ferromagnetism [17,18]. However, the most energetically favorable scenario appears to be the superconducting phase crystal [22,23], a nonuniform superconducting ground state characterized by periodic spontaneous phase gradients. Furthermore, the phase crystal state has gained attention because it remains robust in the presence of strong correlations, disorder, finite-temperature effects [35–37] and provides good agreement with cuprate experiments [35,38–42].

In this work, we investigate prospects for the emergence of nonuniform superconducting ground states, including the phase crystal, in a topological superconductor hosting flat bands of topologically protected Majorana states. This addresses the interplay between, on one hand, forming nonuniform superconducting states to lower the energy and, on the other hand, the topological protection of the Majorana states. We are interested in understanding how the topological protection affects or possibly hinders the emergence of nonuniform superconducting phases. Similar avenues have previously been explored in the context of stability of Majorana states in stacked nanowires [43,44] and small-scale cold-atom systems [45–48]. So-called edge-induced pairing modulations in amplitude [47] and phase [45,46] of the superconducting order parameter have been shown to break symmetries and hybridize Majorana states. Here, we identify these modulations as two different nonuniform superconducting phases, namely, a pair density wave [6,7,49] and a phase crystal [23], and characterize these two states through energy-based arguments and their connection to topology.

To this end, we consider a Majorana flat band model based on atomic spin chains with a helical magnetic texture deposited on an s-wave superconducting substrate [50–57], see Fig. 1. Arrays of such magnetic adatoms have been shown to lead to multiple spin-polarized subgap states that hybridize to form bands [58]. These bands can enter a topologically nontrivial superconducting phase [59–62] supporting flat bands of Majorana edge states protected by chiral symmetry [57,63]. Developments in single-atom manipulation techniques based on scanning tunneling microscopy (STM) have enabled the fabrication, detection, and control of these superconducting subgap states [64–69]. This offers a promising experimental route to realize topological superconductivity in atomic spin

*Contact author: sushanth.varada@physics.uu.se

Published by the American Physical Society under the terms of the Creative Commons Attribution 4.0 International license. Further distribution of this work must maintain attribution to the author(s) and the published article's title, journal citation, and DOI. Funded by Bibsam.

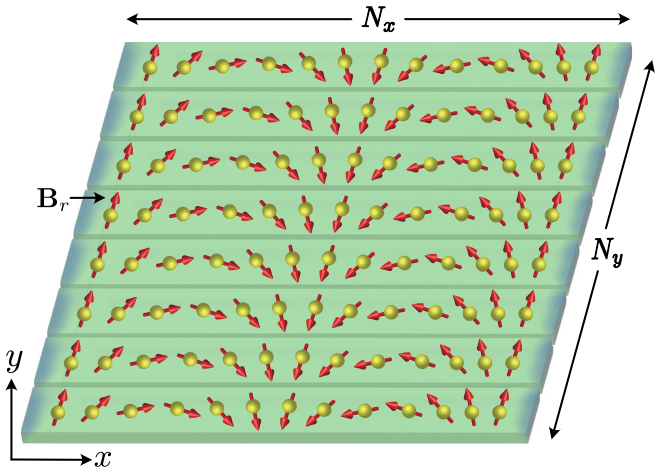


FIG. 1. Schematic illustration of the experimental setup to obtain Majorana flat bands. Magnetic atoms (yellow spheres) with field strength $\mathbf{B}_r$ (red arrows) on an s-wave superconducting substrate (green) are tuned to form coplanar spin spirals with the pitch $\mathbf{q} = (q_x, 0)$. For a wide range of parameters, the system enters a topologically nontrivial regime hosting multiple Majorana edge states along the y direction (schematically illustrated with gray colored cloud). The system consists of $N_x \times N_y$ sites.

chains on a superconductor [70–77]. Specifically, we focus on systems with noncollinear spin spirals in proximity to a conventional superconducting substrate [72,73,77]. To identify the possible ground states in such systems, we start from a tight-binding model for coplanar spin spirals on a two-dimensional (2D) s-wave superconductor [57] and perform self-consistent calculations of the effective superconducting order parameter to find the ground state.

In more detail, we find that the Majorana flat band edge states, present for a uniform superconducting state, are always unstable at low temperatures toward the formation of either a pair density wave or a phase crystal along the edges of the system or the combination thereof. The pair density wave exhibits edge localized superconducting amplitude modulations without any spatial variation in phase. The pair density wave predominantly displays short-range modulations on the atomic scale, even approaching a bond-wave order [46]. In contrast, the phase crystal is characterized by strong superconducting phase modulations at the edges on the superconducting coherence length scale, which drive spontaneous current loops and with only weak modulations in amplitude set by the phase modulation length scale. Both of these nonuniform superconducting states split and shift the Majorana flat band away from zero energy, thereby lowering the overall free energy of the system, but using different mechanisms. The pair density wave appears when sufficient Majorana modes exists with oppositely signed winding numbers, which allow for amplitude modulations through band folding, while the phase crystal appears when one nontrivial winding number is dominating, and thus, instead, phase modulations are needed to gap out the Majorana flat band. Thus, topology, set primarily by the chemical potential, determines which nonuniform state is formed. This results in an experimentally accessible tunability between the pair density wave and the phase crystal.

We find that the pair density wave and phase crystal are roughly as abundant as ground states in the phase diagram, where the order parameter only develops phase modulations when amplitude modulations are not sufficient to shift the Majorana states away from zero energy. In the zero-temperature limit, these two phases are connected by a crossover, where the superconducting order parameter exhibits comparable modulations in amplitude and phase. However, this crossover region diminishes at finite temperatures. The pair density wave also typically exhibits a higher transition temperature, reaching up to around 80% of the mean-field bulk superconducting transition temperature T_c, while the phase crystal survives up to around 10% of T_c. We trace this behavior to the phase crystal only emerging in a parameter regime where both the number of Majorana states and the magnitude of the bulk superconducting gap are relatively small, making it more sensitive to thermal excitations. Above the transition temperatures of these nonuniform superconducting states, the uniform superconducting state with its Majorana flat bands reappears.

The remainder of this work is organized as follows. We discuss the model of the Majorana flat band system and methods used in Sec. II. In Sec. III, we characterize the nonuniform superconducting phases emerging in the zero-temperature limit. This is followed by an analysis of the thermal stability of these phases in Sec. IV. We summarize our results in Sec. V. Appendixes A and B contain details of our derivations, while Appendix C provides additional numerical data.

II. MODEL AND METHODS

A. Magnetic adatoms on conventional superconductor

We consider an array of magnetic impurities deposited onto a conventional s-wave superconducting substrate, as illustrated in Fig. 1. The magnetic adatoms form a spin-polarized band within the superconducting gap, which can be tuned into a topological phase hosting Majorana flat bands [52,55–57,77]. The 2D tight-binding Bogoliubov–de Gennes (BdG) model Hamiltonian of this system in the Nambu basis $\Psi = (c_{r\uparrow}, c_{r\downarrow}, c^\dagger_{r\downarrow}, -c^\dagger_{r\uparrow})^T$ is given by [57]

$$\begin{aligned}\tilde{H} = &\sum_r \Psi_r^\dagger[-\mu\,\tau_z\sigma_0 + \tau_0\,\mathbf{B}_r\cdot\boldsymbol{\sigma}]\Psi_r \\ &+ \sum_r \Psi_r^\dagger\left[-\Delta_r\,\frac{1}{2}(\tau_x + i\tau_y)\sigma_0 + \text{H.c.}\right]\Psi_r \\ &+ \sum_{\langle r,r'\rangle} \Psi_r^\dagger\left[-\frac{t}{2}\,\tau_z\sigma_0\right]\Psi_{r'},\end{aligned} \tag{1}$$

where $c^\dagger_{r\sigma}$ creates an electron on the rth lattice site with spin $\sigma = \uparrow, \downarrow$. Here, $\boldsymbol{\tau}$ and $\boldsymbol{\sigma}$ denote the Pauli matrices acting in particle-hole and spin subspaces, respectively. Furthermore, μ is the chemical potential, and $\mathbf{B}_r = B(\cos\phi_r \sin\varphi_r, \sin\phi_r \sin\varphi_r, \cos\varphi_r)$ represents the effective inhomogeneous magnetic field produced by the magnetic impurities. Here, B is the effective field strength, while ϕ_r and φ_r denote the site-dependent in-plane and out-of-plane angles, respectively. The hopping between the nearest-neighbor lattice sites $\langle r, r'\rangle$ is characterized by t. The s-wave

superconducting order Δ_r, induced by the substrate is a complex quantity with amplitude $|\Delta_r|$ and phase θ_r. The superconducting order parameter is determined self-consistently [78] via

$$\Delta_r = \frac{V}{2}[\langle c_{r\uparrow}c_{r\downarrow}\rangle - \langle c_{r\downarrow}c_{r\uparrow}\rangle] = \frac{V}{2}\sum_{E_n>0}\left[u^n_{r\uparrow}v^{n*}_{r\downarrow} + u^n_{r\downarrow}v^{n*}_{r\uparrow}\right]\tanh\left(\frac{E_n}{2k_BT}\right). \quad (2)$$

Here, $V > 0$ denotes a constant attractive interaction, needed to generate the conventional spin-singlet s-wave superconducting state present in the absence of magnetic impurities, while E_n is the eigenenergy corresponding to the nth eigenstate $(u^n_{r\uparrow}, u^n_{r\downarrow}, v^n_{r\downarrow}, -v^n_{r\uparrow})^T$ of the BdG Hamiltonian in Eq. (1). Furthermore, T is the temperature, and k_B is the Boltzmann constant.

We consider a general class of spin textures on the superconducting substrate with magnetic moments forming coplanar noncollinear spin spirals, as illustrated in Fig. 1 and inspired by recent experimental progress [72,73,77]. This setup generates an in-plane magnetic field with $\varphi_r = \pi/2$ and $\phi_r = 2\pi\,\mathbf{q}\cdot\mathbf{r}$, where $\mathbf{q} = (q_x, q_y)$ denotes the spiral pitch vector. Experimentally, the spiral pitch is a site-dependent quantity, prone to inhomogeneities due to magnetic anisotropy [77]. While mild deviations would retain the noncollinear characteristics of the spin spiral, severe inhomogeneity may be detrimental to the formation of a Majorana flat band. Here, since we are interested in effects due to the existence of a Majorana flat band, we assume a homogeneous spiral pitch as a tunable parameter independent of lattice sites [57].

Next, we perform a local gauge transformation [51,62,78] to remove the site-dependence of the magnetic field (see Appendix A for details) resulting in

$$H = \sum_r \Psi^\dagger_r[-\mu\,\tau_z\sigma_0 + B\,\tau_0\sigma_x]\Psi_r + \sum_r \Psi^\dagger_r\left[-\Delta_r\,\frac{1}{2}(\tau_x + i\tau_y)\sigma_0 + \text{H.c.}\right]\Psi_r + \sum_{\langle r,r'\rangle}\Psi^\dagger_r\left[-\frac{t}{2}\,\tau_z\,\exp(i\sigma_z\pi\,\mathbf{q}\cdot\mathbf{v}_{r,r'})\right]\Psi_{r'}. \quad (3)$$

Here, $\mathbf{v}_{r,r'} = (\delta_{r_x+1,r'_x}, \delta_{r_y+1,r'_y})$ is the real-space vector between the nearest neighbor sites. The exponential phase factor in the kinetic energy generates an effective spin-orbit interaction by coupling the orbital motion to the spin. Importantly, its strength is governed by the spiral pitch $\mathbf{q}$, and unlike the conventional relativistic spin-orbit interaction, this effective coupling is a geometric consequence of the coplanar spiral magnetic moments. Although the conventional spin-orbit coupling in the superconducting substrate is crucial for stabilizing a noncollinear spin spiral ground state [77,79], the model we use does not account for it explicitly. Instead, it relies on the effective spin-orbit interaction generated by the spin spiral to realize topological superconductivity. Including the substrate spin-orbit coupling would only quantitatively modify the topological phase boundaries without changing the underlying topological phase.

B. Topology

The Hamiltonian in Eq. (3) is invariant under effective time-reversal symmetry given by the operator $T = \tau_0\sigma_x\mathcal{K}$, where $\mathcal{K}$ is complex conjugation with T satisfying $T^2 = 1$. Combined with the particle-hole symmetry operator $C = \tau_y\sigma_y\mathcal{K}$, we have the chiral symmetry operator $S = CT = \tau_y\sigma_z$, which anticommutes with the Hamiltonian $\{S, H\} = 0$. These symmetries place the system in the BDI topological class [80,81]. However, the BDI class does not have a topological ground state in 2D. Nevertheless, the Hamiltonian in Eq. (3) can be associated with a weak topological phase [82–84], in which the 2D system is viewed as a composition of parallel one-dimensional (1D) BDI wires characterized by a $\mathbb{Z}$ invariant [85,86]. The chiral symmetry then protects the multiple zero-energy Majorana states (one per wire) on the same edge from hybridizing with each other [63]. This description requires lattice translation symmetry along the edges with the Majorana states. Therefore, even though each 1D BDI wire can host Majorana edge states, both translation and chiral symmetries are required to enable the corresponding 2D system to support Majorana flat bands, see Figs. 3(d) and 3(h) for plots of the Majorana flat band.

To compute the relevant topological number, we perform a Fourier transform of the Hamiltonian in Eq. (3) to obtain

$$H(\mathbf{k}) = \sum_k \Psi^\dagger_k\{[\mathcal{E}(\mathbf{k}) - \mu]\,\tau_z\sigma_0 + B\,\tau_0\sigma_x - \Delta_{\text{bulk}}\,\tau_x\sigma_0 + f(\mathbf{k})\tau_z\sigma_z\}\Psi_k, \quad (4)$$

where $\mathbf{k} = (k_x, k_y)$, $\mathcal{E}(\mathbf{k}) = -t\,\{\cos(\pi q_x)\cos(k_x) + \cos(\pi q_y)\cos(k_y)\}$, and $f(\mathbf{k}) = t\,\{\sin(\pi q_x)\sin(k_x) + \sin(\pi q_y)\sin(k_y)\}$. Here, Δ_{bulk} is the superconducting gap computed self-consistently in k-space by Fourier transforming Eq. (2). For a 1D BDI wire, the topological invariant is an integer winding number [87]. For a 2D lattice with Majorana flat bands along the y direction, see Fig. 1, we can define a k_y-dependent winding number [88–90] as (see Appendix B for details)

$$W(k_y) = -\frac{1}{2}\sum_{f(\mathbf{k})=0}\text{sgn}[\Delta_{\text{bulk}}\,\partial_{k_x}f(\mathbf{k})] \times \text{sgn}\left\{B^2 - [\mathcal{E}(\mathbf{k}) - \mu]^2 - \Delta^2_{\text{bulk}} + f^2(\mathbf{k})\right\}, \quad (5)$$

where the summation is taken for all k_x satisfying the condition $f(\mathbf{k}) = 0$. In 1D wires, the spiral pitch is crucial for tuning the system into a topological phase [55]. Consequently, in a 2D system, the spiral pitch vector $\mathbf{q} = (q_x, q_y)$ influences the number of Majorana states and their stability [57,63]. In this work, we consider $\mathbf{q} = (q_x, 0)$, as a finite q_y component has been found to be detrimental to Majorana flat bands along the y direction [57].

C. Self-consistent calculation of superconductivity

To compute the superconducting order parameter Δ_r self-consistently, we solve the BdG Hamiltonian in Eq. (3) numerically using an iterative scheme on a grid of $N_x \times N_y$ lattice sites. The system is modeled with a cylindrical geometry with open boundary conditions at sites $x = 1, N_x$ and periodic boundary conditions along the y direction. Starting from an initial guess for Δ_r, the Hamiltonian in Eq. (3) is

diagonalized (in the ℓth iteration) to determine the new order parameter $\Delta_r^{(\ell)}$ via Eq. (2). In a standard self-consistent scheme, this updated order parameter yields the next iteration as $\Delta_r^{(\ell+1)} = \mathcal{T}(\Delta_r^{(\ell)})$, where $\mathcal{T}$ encapsulates Hamiltonian reconstruction, diagonalization, and gap recalculation. Convergence is achieved when the maximum change in Δ_r at each site r is below a numerical threshold ϵ between successive iterations. To accelerate this convergence, we employ the Barzilai-Borwein method [91]. This method introduces an adaptive mixing factor $\alpha \in (0.001, 100]$ [92] to update the new order parameter as

$$\Delta_r^{(\ell+1)} = (1-\alpha_{\ell+1})\Delta_r^{(\ell)} + \alpha_{\ell+1}\mathcal{T}\big(\Delta_r^{(\ell)}\big). \tag{6}$$

Here, the mixing factor is updated as $\alpha_{\ell+1} = \alpha_\ell s_\ell$, where $s_\ell = s_\ell^{\text{odd}}$ for odd ℓ and $s_\ell = s_\ell^{\text{even}}$ for even ℓ. These scaling factors depend on the real vector residual $\boldsymbol{\delta}_\ell = \Gamma[\mathcal{T}(\Delta_r^{(\ell)})] - \Gamma[\Delta_r^{(\ell)}]$, where $\Gamma[\bullet]$ stacks the real and imaginary parts (Re[$\bullet$], Im[$\bullet$]). The scaling factors are determined by [92]

$$s_\ell^{\text{odd}} = \frac{\|\boldsymbol{\delta}_{\ell-1}\|_2^2}{|\boldsymbol{\delta}_{\ell-1}\cdot(\boldsymbol{\delta}_\ell - \boldsymbol{\delta}_{\ell-1})|}, \quad s_\ell^{\text{even}} = \frac{|\boldsymbol{\delta}_{\ell-1}\cdot(\boldsymbol{\delta}_\ell - \boldsymbol{\delta}_{\ell-1})|}{\|\boldsymbol{\delta}_\ell - \boldsymbol{\delta}_{\ell-1}\|_2^2}. \tag{7}$$

Self-consistent calculations for each parameter choice were performed with at least three distinct initial guesses of Δ_r. First, we utilize a starting order parameter guess with edge-localized, site-to-site staggered amplitude modulation, and vanishing phase variation as an initial guess for the pair density wave phase. Second, the starting configurations for the phase crystal instead have a uniform amplitude with the ansatz for the phase variation being $\theta(x,y) \propto [1 + x/x_0]e^{-x/x_0}\sin(2\pi n y/N_y)$, adopted from Ref. [23]. Here, we treat x_0 and n as free parameters that govern the phase decay perpendicular to the edge (x direction) and the phase modulation frequency along the edge (y direction), respectively, and we try different frequencies in our initial guesses. Third, we also try uniform solutions. We employ these three unique types of start guesses over the full phase diagram to not bias the outcome. The converged solution with the lowest free energy is then assigned as the ground state. We compute the free energy using $\mathcal{F} = \langle H\rangle - T\mathcal{S}$, where $\langle H\rangle$ corresponds to the internal energy of the Hamiltonian in Eq. (3), and $\mathcal{S}$ is the entropy expressed using the Fermi-Dirac function f_n as $\mathcal{S} = -k_B\sum_n[f_n\ln(f_n) + (1-f_n)\ln(1-f_n)]$ [93].

D. Parameter choices

All energies and temperatures are expressed in units of t, as we set $k_B = 1$. For other parameters, we choose $(N_x, N_y) = (120, 46)$, $\mathbf{q} = (0.3, 0)$, $V = 2t$, and $\epsilon = 10^{-6}$ and compute phase diagrams as functions of chemical potential μ, magnetic field B, and temperature T. For a fixed spiral pitch $\mathbf{q}$, μ and B govern the winding number in Eq. (5), which determines the number of Majorana edge states. We find that this specific pitch value $\mathbf{q}$ supports the topological phase over a wide range of μ and B. A large N_x is chosen to ensure that Majorana states localized at opposite edges of the system remain spatially isolated [72], suppressing finite-size energy splitting caused by wave function overlap [74] between different edges. In fact, in the topologically nontrivial regime, the bulk gap calculated in the finite-size cylinder matches Δ_{bulk} within a 5% relative deviation, indicating that the chosen geometry captures the bulk limit. We note the choice of V produces a relatively large superconducting order parameter Δ, needed to keep the lattice size manageable and still capture the nonuniform superconducting states. Still, since we relate all results to topology and general features, we do not expect any qualitative differences in the presented results for other parameter choices, provided that the system is well within the topological phase hosting Majorana flat bands.

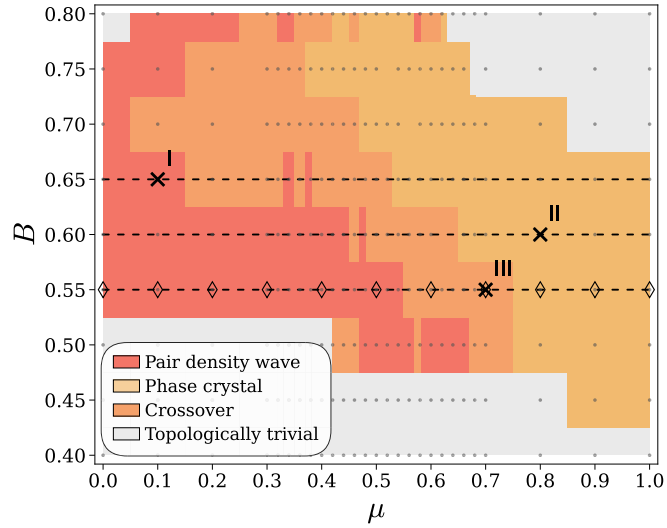


FIG. 2. Ground-state phase diagram as a function of chemical potential μ and magnetic field B at zero temperature. Gray dots indicate the calculated discrete data points. Crosses I, II, and III mark the representative (μ, B) parameters used for discussing the different nonuniform phases throughout Sec. III. Dashed lines indicate values of B used to detail amplitude and phase modulations in Sec. III C. Open diamond markers indicate the value of B used in finite temperature calculations in Sec. IV. Close to the topological phase transitions, an energy landscape riddled with local minima makes it difficult to characterize the true ground state, leading to few point-to-point phase jumps along these boundaries.

III. ZERO-TEMPERATURE PHASES

We first investigate the superconducting phase diagram as a function of chemical potential μ and magnetic field B at zero temperature. The resulting zero-temperature phase diagram is shown in Fig. 2. The red region corresponds to a pair density wave [6,7,49] phase, characterized by clear edge amplitude modulations but no phase variation. This phase breaks lattice translation symmetry along the edges, leading to the hybridization of Majorana states, as we discuss in Sec. III A. Increasing the chemical potential results in a phase crystal [23], denoted by the golden region in the phase diagram. This region instead has dominant phase modulations along the edge with minor accompanying amplitude modulations, as discussed in detail in Sec. III B. The phase crystal breaks chiral symmetry in addition to lattice translation symmetry. Although these two distinct nonuniform phases both differ in the symmetries they break, they share a common feature of lowering the free energy of the system by shifting the Majorana flat bands to finite energies. Furthermore, we find

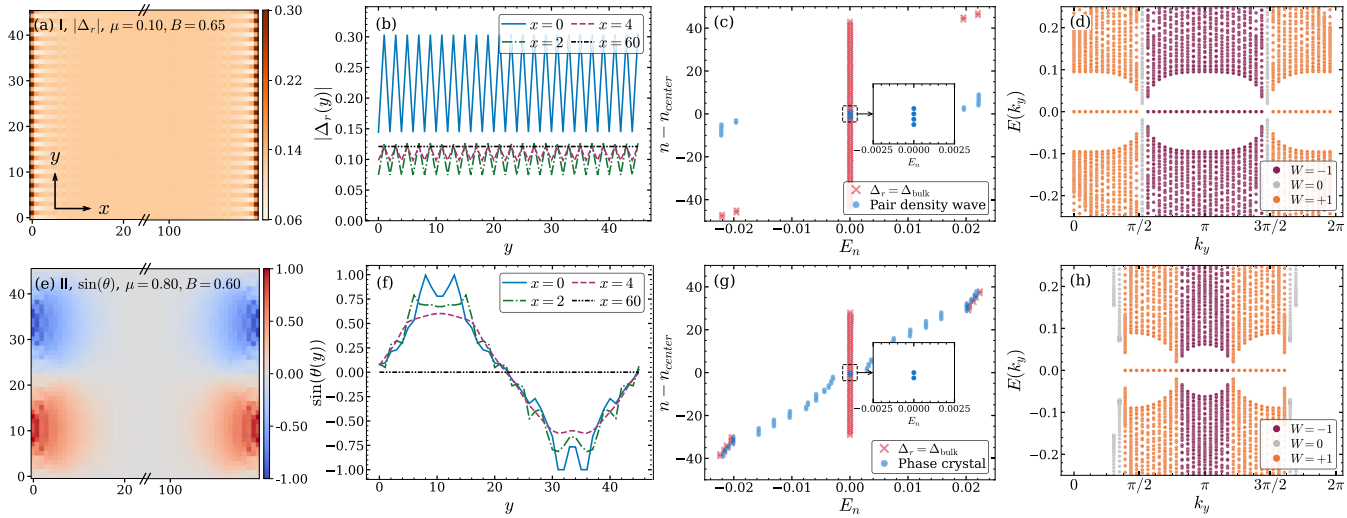


FIG. 3. (top row) (a)–(d) Pair density wave state and (bottom row) (e)–(h) phase crystal state, corresponding to points I at $(\mu, B) = (0.10, 0.65)$ and II at $(\mu, B) = (0.80, 0.60)$ in Fig. 2, respectively. (a) and (e) Color density maps of the superconducting order parameter amplitude $|\Delta_r|$ at I and phase $\sin\theta$ at II, respectively. (b) and (f) Corresponding line plots of the amplitude and the phase modulations as a function of position y along the edge for several fixed values of x, with $x = 0$ being the edge and $x = 60$ representing the bulk. (c) and (g) Low-energy eigenvalues E_n as a function of eigenindex n in pair density wave and phase crystal states (blue dots) compared with the uniform state (red crosses) with $\Delta_r = \Delta_{\rm bulk}$. (d) and (h) Low-energy band structure in a semi-infinite geometry, obtained by a Fourier transform along y with $\Delta_r = \Delta_{\rm bulk}$ as a function of k_y. Colors denote the winding number $W(k_y)$.

a crossover between these two nonuniform phases, shown in orange in the phase diagram. Within this region, we find the ground state to have both finite phase modulations and notable amplitude modulations along the edges. Similar to a phase crystal, this crossover region breaks both translation and chiral symmetries. We detail the characterization of this regime in Sec. III C. Notably, the whole phase diagram is either in the topologically trivial uniform phase (gray) with no Majorana edge states or in the pair density wave, phase crystal, or their crossover at zero temperature, i.e., we find no regime where the Majorana flat band survives, thanks to the superconducting order parameter adopting a highly inhomogeneous pattern near the edges.

A. Pair density wave

We start by examining the properties of the pair density wave, choosing the representative parameters marked by cross I ($\mu = 0.10$ and $B = 0.65$) in Fig. 2. In this state, the amplitude of the superconducting order parameter $|\Delta_r|$ oscillates rapidly along the edges with a large wave vector Q_y, while remaining uniform in the bulk, see Fig. 3(a). However, its phase θ_r remains constant with no spatial variation (see Appendix C). In Fig. 3(b), we extract the amplitude $|\Delta_r|$ along the y direction in regions near the edge ($x = 0, 2, 4$) and in the bulk ($x = 60$). This shows a pair density wave characterized by site-to-site staggered edge amplitude modulations; this is thus a bond-wave order [46]. These amplitude modulations break the translational invariance along the edges of the system, but the chiral symmetry is still preserved, as the lack of phase modulations in the pair density wave leaves the time-reversal symmetry ($T^2 = 1$) unbroken. The finite transverse extent of these amplitude modulations into the bulk also indicates that this is not a strictly 1D phenomenon. The broken translation symmetry is detrimental to the Majorana flat band due to its weak topological protection. In Fig. 3(c), we illustrate this by plotting the distribution of low-energy eigenvalues E_n for both the pair density wave (blue circles) and the uniform superconducting state (red crosses). The latter is obtained by diagonalizing the Hamiltonian in Eq. (3) with a fixed $\Delta_r = \Delta_{\rm bulk}$, the self-consistent bulk superconducting gap. We find that the pair density wave strongly hybridizes most of the Majorana flat band states such that they are removed from zero energy. This lowers the free energy of the system, and since the pair density wave is the ground state for a large range of parameters, the energetic cost of the nonuniform state is clearly outweighed by the gain in free energy from removing these Majorana states.

To understand why the pair density wave forms and favors the bond-wave order configuration, we perform a Fourier transform of the Hamiltonian in Eq. (3) along y with an open boundary condition along x. This results in a set of independent wires of length N_x labeled by momenta $k_y = 2\pi n/N_y$, with $n = 0, 1, \ldots, N_y - 1$. Each k_y-resolved wire can enter the topological phase to host Majorana edge states [44,57], and their band structure with uniform $\Delta_r = \Delta_{\rm bulk}$ is plotted in Fig. 3(d). The colors denote the winding number $W(k_y)$ calculated from Eq. (5). This indicates that the Majorana edge states correspond to $W(k_y) = \pm 1$ and terminate at the gap-closing points with a trivial winding $W(k_y) = 0$ [88,94,95]. Here, chiral symmetry protects the Majorana states with identical windings from coupling with each other [57]. However, states on the same edge with opposite windings are still allowed to hybridize [45,46]. Such a coupling requires scattering between different k_y-resolved wires of opposite windings. The pair density wave exactly enables this scattering by inducing edge-localized amplitude modulations. These modulations have a dominant wave vector Q_y, which corresponds to

the momentum difference between the k_y-resolved wires with opposite windings.

In Fig. 3(d), the wires with $W(k_y) = +1$ can be efficiently coupled to wires with opposite winding if they are scattered by $Q_y = \pi$. This process is enabled by the bond-wave order configuration of the pair density wave, which doubles the unit cell in real-space through its site-to-site staggered modulation of $|\Delta_r|$. The resulting unit cell doubling halves the Brillouin zone, which folds the Majorana flat band onto itself. Consequently, the Majorana states with opposite windings hybridize and open a single uniform gap, as shown in Fig. 3(c). Notably, it is sufficient to modulate the amplitude along the edges, while keeping it constant in the bulk to hybridize the Majorana states, which minimizes the condensation energy cost of amplitude modulations. Our calculations show that the bond-wave order configuration of the pair density wave is largely maintained for $\mu \lessapprox 0.2$. As $|\mu|$ increases, the number of k_y-resolved wires with trivial winding $W = 0$ increases, and folding the Brillouin zone in half is now not energetically sufficient to hybridize the Majorana flat band. The system then instead scatters nontrivial k_y-resolved wires at different values of Q_y rather than a single dominant $Q_y = \pi$. As a result, the pair density wave changes from bond-wave order to a configuration that exhibits a combination of multiple modulation wave vectors, albeit all with short wavelengths. This causes multiple overlapping band foldings in the Brillouin zone. The resulting hybridization of the Majorana flat band leads to subgap states with numerous tiny gap openings.

As the pair density wave relies on coupling Majorana states on the same edge with opposite windings [46], the remnant unhybridized states correspond to the difference $2|W_+ - W_-|$. Here, $W_\pm$ denotes the number of ± 1 winding numbers in the k_y-resolved band structure. The remnant Majorana states remain at zero energy protected by the chiral symmetry. For the representative parameters $(\mu, B) = (0.10, 0.65)$ in Figs. 3(a)–3(d), $W_+ = 21$ and $W_- = 23$, which leaves four Majorana states at zero energy, in agreement with the inset of Fig. 3(c). Generally, in the uniform superconducting state, the maximum number of Majorana states well within the topological phase region is obtained at $\mu = 0$. At this value of μ and for an even N_y, the difference between W_+ and W_- is zero, and the pair density wave thus gaps out all of the Majorana states. In contrast, this difference is one for an odd N_y, leaving a pair of Majorana states at zero energy. To summarize, the pair density wave is driven by the presence of Majorana edge states with different winding numbers. It breaks lattice translation symmetry through edge-localized amplitude modulations such that it gaps out all possible Majorana edge states with opposite winding numbers. We note that this is different from conventional finite-momentum pairing or FFLO pairing [2,3], which is an intrinsic bulk effect or its remnant at a surface [8], found across the superconductor-normal transition and primarily driven by spin splitting of the Fermi surface.

B. Phase crystal

We next investigate the characteristics of the phase crystal for the parameters marked by the cross II ($\mu = 0.80$ and $B = 0.60$) in Fig. 2 and report the details in the bottom panels in Fig. 3. As shown in Figs. 3(e) and 3(f) in this state, the phase θ_r of the superconducting order parameter modulates along the edges but stays uniform in the bulk. The modulation frequency is set by the decay length of the zero-energy states into the bulk, both governed by the superconducting coherence length [23]. Driven by these strong phase modulations, the amplitude $|\Delta_r|$ also acquires a modest spatial variation along the edges that is much weaker and smoother than the pair density wave. Importantly, the modulation length scale of these amplitude modulations is set by the phase modulations. Specifically, the amplitude variation peaks when the phase gradient is zero (see Appendix C for details). The spatially varying phase results in spontaneous superfluid momentum $\mathbf{p}_S \propto \nabla\theta_r$, which nonlocally drive staggered loop currents (see Appendix C) that break both translation and time-reversal symmetries [20–25,35,36,46]. The spontaneous superfluid momentum shifts the Majorana flat band to finite energies, as shown in Fig. 3(g). Formally, such an energy shift is allowed because the phase crystal breaks the chiral symmetry, and without this symmetry, the Majorana states on the same edge may hybridize with each other and shift to finite energies [63]. Although the phase modulations and associated loop currents would increase the free energy of the condensate in the bulk, the existence of zero-energy edge states leads to effectively negative and nonlocal correlations in the superfluid stiffness tensor [23]. This instead favors edge-localized phase gradients that lower the overall free energy of the system. The resulting free energy gain corresponds to shifting the Majorana states away from zero energy.

To understand why the system favors a phase crystal over a pair density wave, we plot the k_y-resolved band structure of the uniform state with $\Delta_r = \Delta_{\text{bulk}}$, in Fig. 3(h). This shows that the flat band of Majorana states is dominated by one nontrivial winding $W_+ \gg W_-$. As the pair density wave relies on scattering between opposite windings, this large imbalance results in many remnant Majorana states. As a consequence, the pair density wave is no longer energetically efficient in hybridizing the Majorana flat bands. Instead, the system forms a phase crystal that spontaneously breaks the chiral symmetry and thereby hybridizes the Majorana states, lowering the free energy. The periodicity of the resulting phase crystal is governed by a delicate balance between the energy gain of phase variations close to the edge due to effectively negative stiffness and the cost of phase variations further from the edge [23]. This balance is also known to be influenced by superconducting coherence length and other relevant system parameters such as finite size [21,24,37]. For instance, at $(\mu, B) = (0.80, 0.50)$ and (0.90,0.55), we obtain a phase crystal instead with six and four phase gradient nodes along y, respectively, as the ground state of the system (see Appendix C for details).

The absence of chiral symmetry for the phase crystal facilitates a pair-wise hybridization of the Majorana states along the same edge. Consequently, the system can only host a maximum of two Majorana states, with one localized on each edge, depending on the parity of the total number of nontrivial k_y-resolved wires, given by $2[(W_+ + W_-) \pmod 2]$. An even number of nontrivial wires leads to an even number of Majorana states along a single edge, which hybridize and gap out completely, while an odd number of nontrivial wires results in one unpaired state surviving on each edge. For the

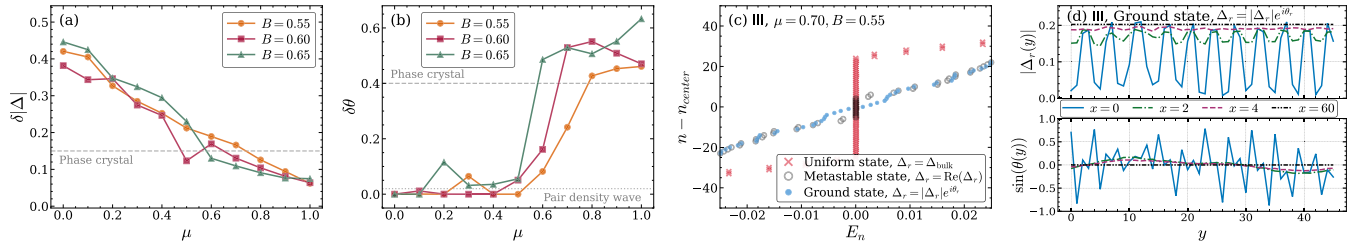


FIG. 4. (a) and (b) Relative change in the superconducting order parameter amplitude $\delta|\Delta|$ and its phase $\delta\theta$, respectively, plotted as a function of chemical potential μ for representative values of B indicated by dashed lines in Fig. 2. (c) Low-energy eigenvalues E_n plotted as a function of eigenindex n corresponding to point III at $(\mu, B) = (0.70, 0.55)$ in Fig. 2. The ground state (blue dots) is compared with the uniform state (red crosses) with $\Delta_r = \Delta_{\text{bulk}}$, and the metastable pair density wave (gray circles) obtained via self-consistent calculations enforcing a real-valued superconducting order parameter. (d) Line plots showing the amplitude modulations (upper panel) and the phase modulations (lower panel) of the ground state at point III as a function of position y along the edge for several fixed values of x, with $x = 0$ being the edge and $x = 60$ representing the bulk.

representative parameters $(\mu, B) = (0.80, 0.60)$, $W_+ + W_- = 11$, which leaves a pair of Majorana states, see inset in Fig. 3(g). A similar odd-even effect arising from hybridization of multiple Majorana bound states has also been reported in Refs. [45,46]. Well within the topological region, we observe that, at $\mu = 1.0$, the sum of W_+ and W_- is even, causing the phase crystal to gap out all Majorana states, regardless of whether N_y is odd or even. To summarize, a phase crystal emerges when the amplitude modulations of a pair density wave are insufficient to hybridize the Majorana flat bands due to a mismatch in the winding numbers. Despite the fact that spontaneous phase modulations and currents usually cost energy in a bulk superconductor, the presence of Majorana edge states at zero energy leads to effectively negative superfluid stiffness correlations [23] such that the edge phase modulations instead minimize the free energy by breaking both translation and chiral symmetries. Hence, weak topology and the winding numbers of Majorana states strongly influence the type of emergent nonuniform superconducting phase.

C. Crossover between pair density wave and phase crystal

We finally discuss the crossover (indicated by the orange area in Fig. 2) from the pair density wave to the phase crystal, driven primarily by increasing $|\mu|$. This region hosts states that inherit characteristics from both superconducting phases. Note that the pair density wave and the phase crystal are distinct phases: They break different symmetries, use different mechanisms to gap out the Majorana flat band to lower the free energy, and have different emergent properties. There is still a crossover region between them that mixes these characteristics. Specifically, the crossover region shows edge-localized modulations of the amplitude $|\Delta_r|$ and phase θ_r, which are weaker than those in the pair density wave and the phase crystal, respectively. To formally characterize this crossover, we investigate the relative changes in the order parameter amplitude $\delta|\Delta|$ and phase $\delta\theta$ along the edge. These quantities are calculated as the spatial average of the root-mean-square (RMS) deviations along y given by $\delta\zeta(\mu, B) = \frac{1}{N}\sum_{x=0}^{N-1}\langle\zeta(x) - \overline{\zeta}(x)\rangle_{\text{rms},y}$, where $\overline{\zeta}$ denotes the arithmetic mean. Here, ζ denotes the normalized amplitude $|\Delta_r|_{\text{norm}} = |\Delta_r|/\Delta_{\text{bulk}}$ or $\sin\theta$. We set the averaging window along x to $N = 3$, as it is sufficient to capture the dominant amplitude and phase modulations. We plot $\delta|\Delta|$ and $\delta\theta$ in Figs. 4(a) and 4(b), respectively, as functions of $|\mu|$ for representative values of B indicated by dashed lines in Fig. 2.

In Figs. 4(a) and 4(b), the discrete data points exhibiting finite amplitude variation $|\delta\Delta| \neq 0$ alongside vanishing phase variations $\delta\theta \approx 0$ characterize the pair density wave. This condition is strictly tied to the topological constraint of nearly balanced opposite windings $W_\pm$, which enables dominant amplitude modulations to hybridize the Majorana flat band, as explained in Sec. III A. Consequently, any parameter regime satisfying this topological constraint will result in a pair density wave with $\delta\theta \approx 0$, corresponding to the dotted gray line in Fig. 4(b). In contrast, the phase crystal, defined in Sec. III B, exhibits strong phase modulations that drive smooth amplitude variations along the edge, such that $\delta\theta > \delta|\Delta|$. Because the pair density wave cannot efficiently hybridize a Majorana flat band with large imbalance between opposite windings $W_\pm \gg W_\mp$, the phase crystal emerges in this parameter regime to lower the free energy of the system. However, due to the crossover between the two nonuniform states, defining a quantitative boundary for dominant phase modulations depends on the parameter regime. Nonetheless, the qualitative features of a phase crystal remain unchanged [23]. For our choice of parameters, we define the phase crystal by $\delta\theta > 0.4$ (representing 40% of the maximum phase $|\sin\theta|_{\max} = 1$), while the corresponding amplitude variations $\delta|\Delta|$ remain roughly below 0.15 (representing 15% of the normalized bulk value $|\Delta_{\text{bulk}}|_{\text{norm}} = 1$), see gray dashed lines in Figs. 4(a) and 4(b). Given these criteria, we can then define the crossover as the region where the relative change in phase modulations remains below 40% and the amplitude modulations roughly exceed 15% of the normalized bulk gap [96]. We note that any changes to the numerical bounds of the phase crystal that align with its defining topological constraints will only shift the crossover boundary internally, without any qualitative changes to the overall phase diagram.

We attribute the existence of the crossover region to remnant Majorana states with identical windings that cannot hybridize within the pure pair density wave state. Typically, the imbalance between W_+ and W_- increases with increasing $|\mu|$. Here, the system develops finite phase modulations in addition to existing amplitude modulations of the pair density wave to hybridize the remnant Majorana states. This further

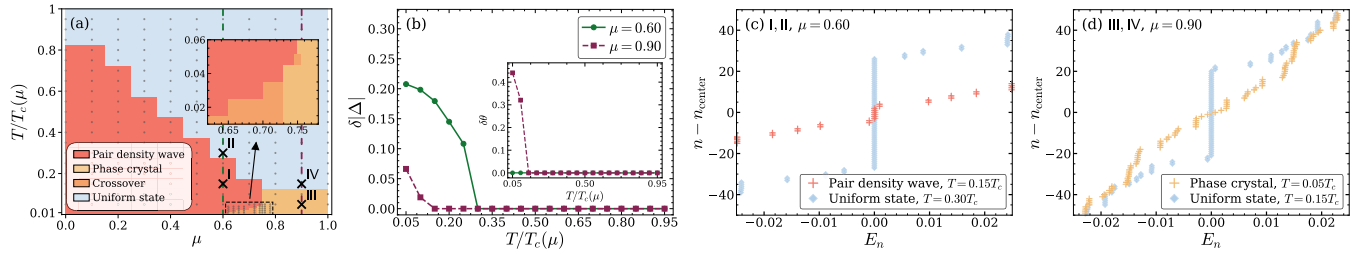


FIG. 5. (a) Ground-state phase diagram as a function of chemical potential μ and temperature T at $B = 0.55$. Here, T is normalized by the bulk superconducting transition temperature $T_c(\mu)$. Gray dots indicate the calculated discrete data points. The inset shows the small area occupied by the crossover region between pair density wave and phase crystal. (b) Relative change in the superconducting order parameter amplitude $\delta|\Delta|$ and its phase $\delta\theta$ (inset) plotted as a function of normalized temperature $T/T_c(\mu)$ for fixed values of chemical potential μ indicated by the dashed lines in (a). Panels (c) and (d) show low-energy eigenvalues E_n plotted as a function of eigenindex n for $\mu = 0.60$, $T = 0.15T_c, 0.30T_c$ [I, II in (a)] and $\mu = 0.90$, $T = 0.05T_c, 0.15T_c$ [III, IV in (a)], respectively.

reduces the free energy of the system, resulting in a crossover where both amplitude and phase modulations coexist on a rather equal footing. To confirm this, we performed additional self-consistent calculations in the crossover region by restricting the order parameter to be real valued, allowing only for amplitude variations. These calculations result in a metastable pair density wave with higher free energy than the ground state. The low-energy eigenvalues E_n at the representative parameters $\mu = 0.70$ and $B = 0.55$ marked by the cross III in Fig. 2, are shown in Fig. 4(c). This clearly shows how the real-valued metastable solution (gray circles) still hosts some Majorana states, although substantially reduced from the uniform $\Delta_r = \Delta_{\text{bulk}}$ (red crosses). In contrast, the ground state of the system (blue dots) gaps out these remnant Majorana states with both amplitude and phase modulations, as shown in Fig. 4(d), to further lower the free energy.

It has previously been interpreted [46,57] that pure amplitude modulations ($\delta\theta \approx 0$) appear only at $\mu = 0$. The authors of these studies further suggested that, for increasing N_y, the system would generally prefer to gap out the Majorana flat bands through phase oscillations ($\delta\theta \neq 0$). However, we perform additional calculations on a $(N_x, N_y) = (60, 80)$ lattice and find that the zero-temperature phase diagram qualitatively remains unchanged even for larger N_y. Additional numerical checks, presented in Appendix D, show that the pair density wave, phase crystal, and their crossover remain stable for larger N_y. Hence, our results clarify that, for a weak topological superconductor in the BDI class, dominant amplitude modulations (pair density wave: $\delta|\Delta| > 0, \delta\theta \approx 0$) and phase modulations (phase crystal: $\delta\theta > \delta|\Delta|$) represent two different nonuniform superconducting phases that emerge to reduce the free energy of the system but through different mechanisms.

IV. TEMPERATURE-DEPENDENT PHASE DIAGRAM

Having studied the two nonuniform superconducting phases at zero temperature, we next investigate their finite-temperature behavior within the mean-field approximation. We show the ground-state phase diagram as a function of temperature and chemical potential μ in Fig. 5(a). The temperature T is normalized by $T_c(\mu)$, which is the bulk superconducting transition temperature. These results are calculated for the representative value $B = 0.55$, indicated by the open diamond markers in Fig. 2. Numerical checks at different B show no qualitative changes in temperature behavior, beyond the phase crystal appearing as the ground state at lower values of μ at higher B. Unlike the zero-temperature limit, the finite-temperature phase diagram features the topologically nontrivial uniform phase with Majorana flat band as a self-consistent solution appearing at sufficiently high temperatures, while the crossover region between the pair density wave and the phase crystal substantially diminishes.

In Fig. 5(a), the boundary between the pair density wave and the (self-consistent) uniform state solution sets a transition temperature $T^*_{\text{PDW}}(\mu)$. This value decreases linearly from around 80% of the bulk transition temperature at $\mu = 0.0$ to around 10% at $\mu \approx 0.75$. This behavior of $T^*_{\text{PDW}}(\mu)$ follows the monotonic weakening of the amplitude modulations $\delta|\Delta|$ with increasing $|\mu|$, as already seen in Fig. 4(a). Furthermore, we compute the mean RMS deviations $\delta|\Delta|$ and $\delta\theta$ as a function of T/T_c at $\mu = 0.60$, indicated by a dashed green line in Fig. 5(a), to analyze the transition of the pair density wave to the uniform state solution in Fig. 5(b) (solid green line). Here, $\delta|\Delta|$ exhibits a monotonic decrease with increasing temperature, while $\delta\theta$ remains zero throughout the transition, as expected. In Fig. 5(c), we also plot the distribution of low-energy eigenvalues E_n at the same $\mu = 0.60$ for the two temperatures corresponding to crosses I and II in Fig. 5(a). Above $T > T^*_{\text{PDW}}$, the system hosts the full Majorana flat band, but below T^*_{PDW}, only the remnant Majorana states from the pair density wave survive. The transition temperature of the phase crystal T^*_{PC} remains at 10% of the bulk $T_c(\mu)$ throughout the phase diagram where it exists in Fig. 5(a). However, depending on system parameters, e.g., in systems with an effectively shorter coherence length, the transition temperature T^*_{PC} has previously been shown to be significantly enhanced above 20–30% of the bulk T_c [24,35]. The mean RMS deviations at $\mu = 0.90$, indicated by the dashed maroon line in Fig. 5(a), are plotted in Fig. 5(b) and show that $\delta\theta$ decreases with increasing temperature. Since chiral symmetry remains broken throughout $T < T^*_{\text{PC}}$, the Majorana flat band reappears only when $\delta\theta$ vanishes above T^*_{PC}, as illustrated by the low-energy eigenvalues in Fig. 5(d), corresponding to the crosses III and IV in Fig. 5(a).

Furthermore, we find that the crossover between the pair density wave and the phase crystal occupies a considerably smaller area in the finite-temperature phase diagram, as shown in the inset of Fig. 5(a). Our calculations show that the crossover region persists only up to approximately 4–5% of the bulk $T_c(\mu)$. This, combined with the lower transition temperature of the phase crystal, suggests that phase modulations are more sensitive to thermal effects than the amplitude modulations. We can attribute this fragility at finite temperatures to at least two effects. First, as $|\mu|$ increases, the number of Majorana states decreases. This leads to a suppression of all emergent nonuniform phases. Second, the superconducting bulk gap Δ_{bulk} decreases with increasing $|\mu|$ and B. At finite temperatures, this facilitates the thermal occupation of states above zero energy, thereby diminishing the free energy gain obtained by shifting the zero-energy edge states. As the phase θ_r modulated regime in the zero-temperature phase diagram occupies regions of relatively high μ and B, it thereby becomes more sensitive to temperature effects.

V. SUMMARY AND OUTLOOK

In this work, we examine the mean-field thermodynamic instabilities of a 2D Majorana flat band model toward inhomogeneous superconducting ground states. We study a tight-binding model of a helical spin chain on an s-wave superconductor with chiral symmetry, belonging to the BDI topological class [57]. This system supports a weak topological phase [82–84] in the form of a translationally invariant stack of 1D BDI wires, each characterized by a winding number. Authors of earlier studies on such models have shown that pairing modulations in the superconducting order parameter were detrimental to the stability of Majorana flat bands [43–48]. We clarify that these modulations are two different symmetry-breaking nonuniform superconducting ground states, a pair density wave and a phase crystal, that minimize the free energy by removing the zero-energy Majorana states using different mechanisms. The pair density wave state breaks translational invariance via amplitude $|\Delta_r|$ modulations without any phase θ_r modulations. This state allows for hybridization of Majorana states with different winding numbers, thereby removing them from zero energy. In contrast, the phase crystal exhibits a spatially varying phase θ_r that breaks both translation and chiral symmetries, with only accompanied small amplitude modulations driven by the varying phase. The phase variations correspond to a finite superfluid momentum that shifts the Majorana states to finite energies and drives spontaneous currents. Overall, the competition between these nonuniform phases is governed by the winding numbers of the constituent 1D BDI wires, which primarily depend on the chemical potential. In the zero-temperature limit, we find that these two phases are bridged by a crossover region, where the order parameter has comparable modulations in both amplitude and phase, where Majorana states are effectively removed by both hybridization and shifted due to spontaneous superfluid momentum.

At finite temperature, we find that the nonuniform phases exhibit distinct transition temperatures to the uniform state, hosting the Majorana flat band. Specifically, the pair density wave transition temperature decreases from 80% to 10% of T_c as the chemical potential potential increases, a trend consistent with the weakening amplitude variations $\delta|\Delta|$ observed in the zero-temperature limit. The transition temperature for the phase crystal remains approximately 10% of T_c throughout the phase diagram. Based on previous studies, we expect that the phase crystal transition temperature can be substantially enhanced, e.g., in systems with an effectively shorter coherence length [24,35], making it significantly more competitive. The crossover region occupies a much smaller region in the finite-temperature phase diagram. We attribute the relative thermal instability of the phase modulations to a relatively lower number of Majorana states and a smaller superconducting bulk gap.

The broader message in this work is that the Majorana flat bands in at least a weak topological superconductor are extremely unstable toward spatial modulations of the superconducting order parameter. We find that the order parameter easily modulates its amplitude $|\Delta_r|$ and its phase θ_r when the amplitude modulations are insufficient to remove the Majorana flat band. Their dependence on winding numbers shows that the underlying topology dictates the nature of the emergent nonuniform superconducting phase. Therefore, systems with Majorana flat bands become a natural playground for strongly nonuniform superconducting states.

A natural follow up of our work is investigating the effects of time-reversal invariant disorder. While such disorder keeps the system within the BDI class, leaving the Majorana flat bands intact [57], its impact on the emergent nonuniform superconducting ground states is yet to be studied. Additionally, our finite-temperature mean-field calculations do not account for possible additional effects due to thermal phase fluctuations, which needs further investigation. Moreover, our work only considers a weak topological system with lattice translation and chiral symmetries. Exploring systems across different topological classes with stronger symmetries protecting the Majorana flat bands not only broadens our understanding of the interplay between energy minimization and topology but also provides insights into the stability of Majorana states. For example, it has been demonstrated that imposing mirror symmetry protects degenerate Majorana Kramers pairs against inhomogeneities of the order parameter in the s-wave superfluid belonging to the DIII topological class [48]. Another complementary direction to assess the interplay between spontaneous symmetry-breaking, interactions, and topology might be provided by the generalized Landau paradigm [97].

ACKNOWLEDGMENTS

We acknowledge A. Theiler and A. K. Ghosh for helpful discussions. We acknowledge financial support from the European Union through the European Research Council (ERC) under the European Union's Horizon 2020 research and innovation programme (ERC-2022-CoG, Grant Agreement No. 101087096). Views and opinions expressed are, however, those of the authors only and do not necessarily reflect those of the European Union or the European Research Council Executive Agency. Neither the European Union nor the granting authority can be held responsible for them. The

computations were enabled by the Berzelius resource provided by the Knut and Alice Wallenberg Foundation at the National Supercomputer Centre. Additional computations and data handling were enabled by resources provided by the National Academic Infrastructure for Supercomputing in Sweden (NAISS) at NSC, UPPMAX, PDC, and HPC2N, partially funded by the Swedish Research Council through Grant Agreement No. 2022-06725. We further acknowledge NAISS for awarding this project access to the LUMI supercomputer, owned by the EuroHPC Joint Undertaking and hosted by CSC (Finland) and the LUMI consortium.

DATA AVAILABILITY

The data that support the findings of this article are openly available [98].

APPENDIX A: GAUGE TRANSFORMATION INTRODUCING THE EFFECTIVE SPIN-ORBIT COUPLING

We apply a local gauge transformation $\Psi_r \to U_r\Psi_r$ to the Hamiltonian in Eq. (1) using the unitary operator $U_r = \tau_0 \exp[i(\phi_r/2)\sigma_z]$ to obtain

$$H = \sum_r \Psi_r^\dagger \left[-\mu\, \tau_z\sigma_0 + B\,\tau_0\sigma_x + \left(-\Delta_r \frac{1}{2}(\tau_x + i\tau_y)\sigma_0 + \text{H.c.} \right) \right] \Psi_r - \frac{t}{2} \sum_{\langle r,r'\rangle} \Psi_r^\dagger [\tau_z\, e^{-i(\phi_r/2)\sigma_z} \sigma_0 e^{i(\phi_{r'}/2)\sigma_z}] \Psi_{r'}. \tag{A1}$$

This transformation aligns the spin at each site with the x axis of the local spin basis [51,62,78]. To proceed, we focus on the gauge transformation that acts in the spin subspace of the kinetic term

$$\begin{aligned} \sum_{\langle r,r'\rangle} e^{-i(\phi_r/2)\sigma_z} \sigma_0 e^{i(\phi_{r'}/2)\sigma_z} &= \sum_{\langle r,r'\rangle} \sigma_0 \exp\left[-\frac{i\sigma_z}{2}(\phi_r - \phi_{r'}) \right] = \sum_{\langle r,r'\rangle} \sigma_0 \exp\left[\frac{i\sigma_z}{2}(2\pi q_x[r'_x - r_x] + 2\pi q_y[r'_y - r_y]) \right] \\ &= \sum_{\langle r,r'\rangle} \sigma_0 \exp[i\sigma_z \pi (q_x \delta_{r_x+1,r'_x} + q_y \delta_{r_y+1,r'_y})] = \sum_{\langle r,r'\rangle} \sigma_0 \exp[i\sigma_z \pi\, \mathbf{q}\cdot\mathbf{v}_{r,r'}], \end{aligned} \tag{A2}$$

where $\mathbf{q} = (q_x, q_y)$ is the spiral pitch between adjacent spins and $\mathbf{v}_{r,r'} = (\delta_{r_x+1,r'_x}, \delta_{r_y+1,r'_y})$ is the real-space vector between the nearest neighbors $\langle r, r'\rangle$. The modified kinetic term is thus given by

$$H_{\text{kin}} = \sum_{\langle r,r'\rangle} \Psi_r^\dagger \left[-\frac{t}{2}\, \tau_z\, \exp(i\sigma_z \pi\, \mathbf{q}\cdot\mathbf{v}_{r,r'}) \right] \Psi_{r'} \tag{A3}$$

$$= \sum_{\langle r,r'\rangle} \Psi_r^\dagger \left[-\frac{t}{2}\, \tau_z\sigma_0 \cos(\pi\, \mathbf{q}\cdot\mathbf{v}_{r,r'}) - \frac{t}{2}\, \tau_z\, i\sigma_z \sin(\pi\, \mathbf{q}\cdot\mathbf{v}_{r,r'}) \right] \Psi_{r'}, \tag{A4}$$

where the sinusoidal component gives an effective spin-orbit interaction and the cosine term modifies the hopping between lattice sites. By substituting Eq. (A3) into Eq. (A1), we obtain the Hamiltonian in Eq. (3) in the main text.

APPENDIX B: DERIVATION OF WINDING NUMBER

For the k-space Hamiltonian $H(\mathbf{k})$ in Eq. (4), the k_y-dependent winding number is given by an integral over k_x as [88–90]

$$W(k_y) = -\frac{1}{4\pi i} \int_0^{2\pi} dk_x \text{tr}[SH^{-1}(\mathbf{k})\partial_{k_x} H(\mathbf{k})]. \tag{B1}$$

By choosing a basis in which the chiral symmetry operator S is diagonal in the particle-hole subspace, the anticommutation $\{S, H\} = 0$ implies that the Hamiltonian must take a block off-diagonal form

$$S = \begin{pmatrix} \sigma_0 & 0 \\ 0 & -\sigma_0 \end{pmatrix}, \quad H(\mathbf{k}) = \begin{pmatrix} 0 & A(\mathbf{k}) \\ A^\dagger(\mathbf{k}) & 0 \end{pmatrix}.$$

Consequently, $W(k_y)$ can be expressed in terms of $A(\mathbf{k})$ as

$$W(k_y) = \frac{1}{2\pi} \text{Im} \left[\int_0^{2\pi} dk_x \partial_{k_x} \ln \det A(\mathbf{k}) \right]. \tag{B2}$$

To determine $A(\mathbf{k})$, we thus transform the k-space Hamiltonian in Eq. (4) into a block off-diagonal form in the particle-hole subspace using the unitary operator

$$U = \frac{1}{2}(\tau_0\sigma_a + \tau_x\sigma_a^* + i\tau_y\sigma_b^* + \tau_z\sigma_b), \quad \text{where} \quad \sigma_a = e^{i(\pi/4)} \begin{bmatrix} 1 & 1 \\ 0 & 0 \end{bmatrix}, \quad \sigma_b = e^{i(\pi/4)} \begin{bmatrix} 0 & 0 \\ -1 & 1 \end{bmatrix}.$$

The transformed Hamiltonian is then

$$U^\dagger H(\mathbf{k}) U = \begin{bmatrix} 0 & \Delta_{\text{bulk}}\,\sigma_x - i[(\mathcal{E}(\mathbf{k}) - \mu)\,\sigma_0 + B\,\sigma_z + f(\mathbf{k})\,\sigma_x] \\ \Delta_{\text{bulk}}\,\sigma_x + i[(\mathcal{E}(\mathbf{k}) - \mu)\,\sigma_0 + B\,\sigma_z + f(\mathbf{k})\,\sigma_x] & 0 \end{bmatrix}, \tag{B3}$$

which gives $A(\mathbf{k}) = \Delta_{\text{bulk}}\,\sigma_x - i[(\mathcal{E}(\mathbf{k}) - \mu)\,\sigma_0 + B\,\sigma_z + f(\mathbf{k})\,\sigma_x]$.

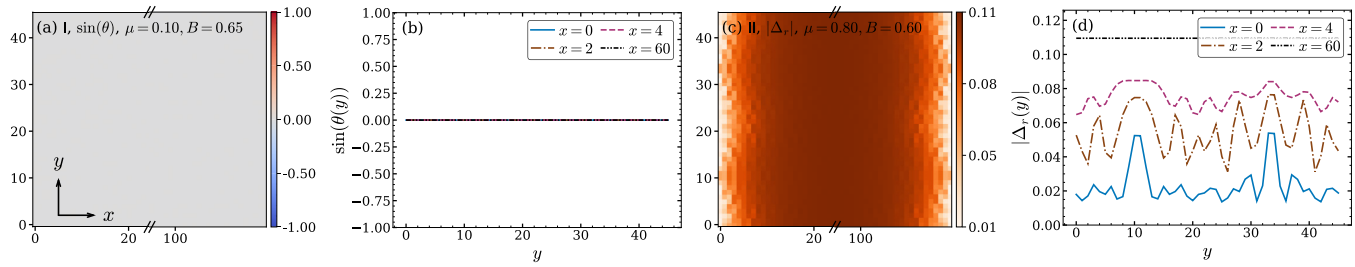


FIG. 6. (a) and (b) Pair density wave state and (c) and (d) phase crystal state, corresponding to points I at $(\mu, B) = (0.10, 0.65)$ and II at $(\mu, B) = (0.80, 0.60)$, in Fig. 2, respectively. (a) and (c) Color density maps of the superconducting order parameter phase $\sin\theta$ at I and amplitude $|\Delta_r|$ at II, respectively. (b) and (d) Corresponding line plots of the phase modulations and the amplitude modulations as a function of position y along the edge for several fixed values of x with $x = 0$ being the edge and $x = 60$ the bulk.

Next, by following the procedure outlined in Ref. [88], we evaluate the integral in Eq. (B2) with $\det A(\mathbf{k}) = B^2 - [\mathcal{E}(\mathbf{k}) - \mu]^2 - [\Delta_{\text{bulk}} - if(\mathbf{k})]^2$. For brevity, we set $T(\mathbf{k}) = \mathcal{E}(\mathbf{k}) - \mu$. This gives

$$W(k_y) = \frac{1}{2\pi}\text{Im}\left[\int_0^{2\pi} dk_x \partial_{k_x} \ln\left[B^2 - T^2(\mathbf{k}) - \Delta_{\text{bulk}}^2 + f^2(\mathbf{k}) - 2i\Delta_{\text{bulk}} f(\mathbf{k})\right]\right] \tag{B4}$$

$$= \frac{1}{2\pi}\int_0^{2\pi} dk_x \frac{2\Delta_{\text{bulk}} f(\mathbf{k})\partial_{k_x}\left[B^2 - T^2(\mathbf{k}) - \Delta_{\text{bulk}}^2 + f^2(\mathbf{k})\right] - \left[B^2 - T^2(\mathbf{k}) - \Delta_{\text{bulk}}^2 + f^2(\mathbf{k})\right]\partial_{k_x}[2\Delta_{\text{bulk}} f(\mathbf{k})]}{\left[B^2 - T^2(\mathbf{k}) - \Delta_{\text{bulk}}^2 + f^2(\mathbf{k})\right]^2 + [2\Delta_{\text{bulk}} f(\mathbf{k})]^2}. \tag{B5}$$

Since the winding number is invariant under continuous transformations, we may rescale either term in the denominator of the integrand to determine the leading order contribution to Eq. (B5). For simplicity, we rescale Δ_{bulk} by taking $\Delta_{\text{bulk}} \to \epsilon\Delta_{\text{bulk}}$, where ϵ is a small positive constant. This gives

$$W(k_y) = \frac{1}{2\pi}\int_0^{2\pi} dk_x \frac{2\epsilon\Delta_{\text{bulk}} f(\mathbf{k})\partial_{k_x}[B^2 - T^2(\mathbf{k}) - (\epsilon\Delta_{\text{bulk}})^2 + f^2(\mathbf{k})] - [B^2 - T^2(\mathbf{k}) - (\epsilon\Delta_{\text{bulk}})^2 + f^2(\mathbf{k})]\partial_{k_x}[2\epsilon\Delta_{\text{bulk}} f(\mathbf{k})]}{[B^2 - T^2(\mathbf{k}) - (\epsilon\Delta_{\text{bulk}})^2 + f^2(\mathbf{k})]^2 + [2\epsilon\Delta_{\text{bulk}} f(\mathbf{k})]^2}. \tag{B6}$$

Here, the integrand sharply peaks near the zeros k_x^0 of the denominator $B^2 - T^2(\mathbf{k}) + f^2(\mathbf{k})$. Hence, in the limit of small $\epsilon\Delta_{\text{bulk}}$, the dominant contribution to the integral comes from the neighborhood δ of these points, and the winding number is given by the sum of the contributions from all such zeros. By expanding the functions in the integral Eq. (B6) near k_x^0, satisfying the condition $B^2 - T^2(k_x^0, k_y) + f^2(k_x^0, k_y) = 0$, we arrive at the lowest order nonvanishing terms

$$B^2 - T^2(\mathbf{k}) - (\epsilon\Delta_{\text{bulk}})^2 + f^2(\mathbf{k}) \approx \partial_{k_x}[B^2 - T^2(k_x, k_y) - (\epsilon\Delta_{\text{bulk}})^2 + f^2(k_x, k_y)]|_{k_x = k_x^0}\left(k_x - k_x^0\right) + \cdots, \tag{B7}$$

$$f(\mathbf{k}) = f(k_x^0, k_y) + \cdots. \tag{B8}$$

As the term $\partial_{k_x}[2\epsilon\Delta_{\text{bulk}} f(k_x^0, k_y)] = 0$, the winding number can be estimated as

$$W(k_y) = \sum_{k_x^0}\frac{1}{2\pi}\int_{k_x^0-\delta}^{k_x^0+\delta} dk_x \frac{2\epsilon\Delta_{\text{bulk}} f\left(k_x^0, k_y\right)\partial_{k_x}\left[B^2 - T^2\left(k_x^0, k_y\right) - (\epsilon\Delta_{\text{bulk}})^2 + f^2\left(k_x^0, k_y\right)\right]}{\left\{\partial_{k_x}\left[B^2 - T^2\left(k_x^0, k_y\right) - (\epsilon\Delta_{\text{bulk}})^2 + f^2\left(k_x^0, k_y\right)\right]\right\}^2\left(k_x - k_x^0\right)^2 + \left[2\epsilon\Delta_{\text{bulk}} f\left(k_x^0, k_y\right)\right]^2}. \tag{B9}$$

Now, setting the constant $\eta_{k_x^0} = \partial_{k_x}[B^2 - T^2(k_x, k_y) - (\epsilon\Delta_{\text{bulk}})^2 + f^2(k_x, k_y)]|_{k_x = k_x^0}$ for brevity and upon a change of variable $z = (k_x - k_x^0)$, we obtain

$$W(k_y) = \sum_{k_x^0}\frac{2\epsilon\Delta_{\text{bulk}} f\left(k_x^0, k_y\right)\eta_{k_x^0}}{2\pi}\int_{-\delta}^{\delta} dz \frac{1}{\eta_{k_x^0}^2 z^2 + \left[2\epsilon\Delta_{\text{bulk}} f\left(k_x^0, k_y\right)\right]^2} = \sum_{k_x^0}\frac{1}{\pi}\tan^{-1}\left(\frac{\eta_{k_x^0}\delta}{2\epsilon\Delta_{\text{bulk}} f\left(k_x^0, k_y\right)}\right). \tag{B10}$$

As the numerator is dominated by the leading-order term $\eta_{k_x^0}\delta \gg 2\epsilon\Delta_{\text{bulk}} f(k_x^0, k_y)$, the argument of the arctangent approaches infinity. By setting the positive constant ϵ to unity, the winding number can be written as

$$W(k_y) = \frac{1}{2}\sum_{k_x^0}\text{sgn}\left\{\partial_{k_x}\left[B^2 - T^2(k_x, k_y) - \Delta_{\text{bulk}}^2 + f^2(k_x, k_y)\right]\big|_{k_x = k_x^0}\right\}\text{sgn}\left[\Delta_{\text{bulk}} f\left(k_x^0, k_y\right)\right], \tag{B11}$$

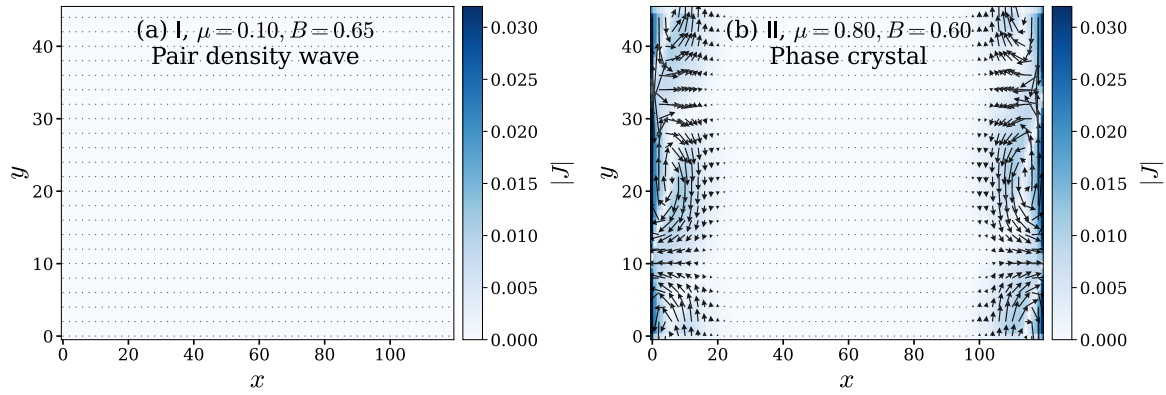


FIG. 7. (a) and (b) Color density maps of the magnitude of current vector field $|J|$ and the corresponding vector plots for pair density wave state at I, $(\mu, B) = (0.10, 0.65)$ and for phase crystal state at II, $(\mu, B) = (0.80, 0.60)$, in Fig. 2, respectively.

where k_x^0 are the points that satisfy the condition $B^2 - T^2(k_x^0, k_y) + f^2(k_x^0, k_y) = 0$, at fixed values of k_y. An equivalent expression for the winding number can be obtained by scaling the term $[B^2 - T^2(\mathbf{k}) - \Delta_{\text{bulk}}^2 + f^2(\mathbf{k})]$ with ϵ instead of Δ_{bulk} in the denominator of the integrand in Eq. (B5). Following the same procedure, this effectively interchanges the roles of $\Delta_{\text{bulk}} f(k_x^0, k_y)$ and $B^2 - T^2(k_x, k_y) - \Delta_{\text{bulk}}^2 + f^2(k_x, k_y)$ in Eq. (B11) giving

$$W(k_y) = -\frac{1}{2} \sum_{k_x^0} \text{sgn}\{\partial_{k_x}[\Delta_{\text{bulk}} f(k_x, k_y)]|_{k_x = k_x^0}\} \text{sgn}\big[B^2 - T^2\big(k_x^0, k_y\big) - \Delta_{\text{bulk}}^2 + f^2\big(k_x^0, k_y\big)\big], \tag{B12}$$

where k_x^0 are now the points that satisfy the condition $f(k_x^0, k_y) = 0$, at fixed values of k_y. The expression in Eq. (B12) provides a simple and straightforward evaluation of the winding numbers. By further rewriting, we finally arrive at

$$W(k_y) = -\frac{1}{2} \sum_{f(\mathbf{k})=0} \text{sgn}[\Delta_{\text{bulk}}\, \partial_{k_x} f(\mathbf{k})] \text{sgn}\big\{B^2 - [\mathcal{E}(\mathbf{k}) - \mu]^2 - \Delta_{\text{bulk}}^2 + f^2(\mathbf{k})\big\}, \tag{B13}$$

which is given as Eq. (5) in the main text.

APPENDIX C: ADDITIONAL DATA FOR PAIR DENSITY WAVE AND PHASE CRYSTAL

Figures 6(a) and 6(b) show the vanishing phase modulations of the pair density wave at point I in Fig. 2, corresponding to the parameters $\mu = 0.10, B = 0.65$, as discussed in Sec. III A. Similarly, Figs. 6(c) and 6(d) depict the weak amplitude modulations driven by the phase crystal at point II in Fig. 2 for the parameters $\mu = 0.80, B = 0.60$, as discussed in Sec. III B. Figure 7(a) shows the absence of currents in the pair density wave state at point I due to lack of phase modulations. In contrast, Fig. 7(b) shows the spontaneous staggered loop currents in the phase crystal state at point II that break both translation and time-reversal symmetries, as discussed in Sec. III B. Furthermore, to provide an overview of different phase crystal configurations obtained as ground states at zero temperature, we present additional representative data in Fig. 8 at two other points in the phase diagram, as discussed in Sec. III B.

APPENDIX D: ADDITIONAL DATA FOR LATTICE SIZES WITH FIXED N_x AND VARYING N_y

For a few representative parameters in the zero-temperature phase diagram (Fig. 2), we perform additional

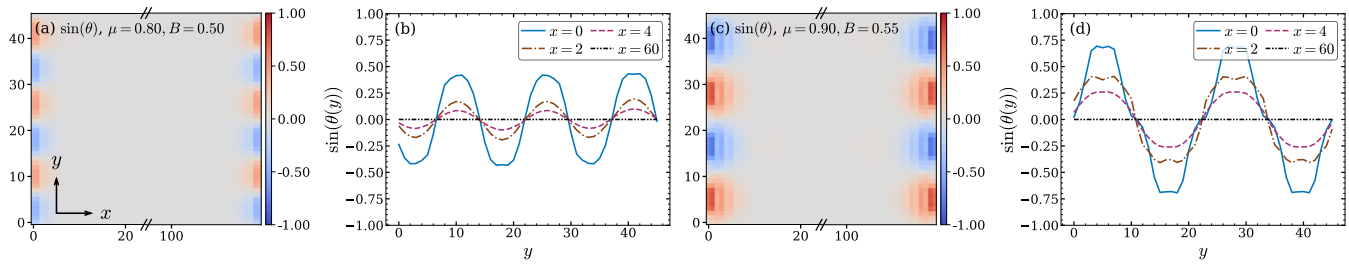


FIG. 8. Additional data in the phase crystal state at zero temperature. (a) and (c) Color density maps of the superconducting order parameter phase $\sin\theta$ at $(\mu, B) = (0.80, 0.50)$ and $(0.90, 0.55)$, in Fig. 2, respectively. (b) and (d) Corresponding line plots as a function of position y along the edge for several fixed values of x.

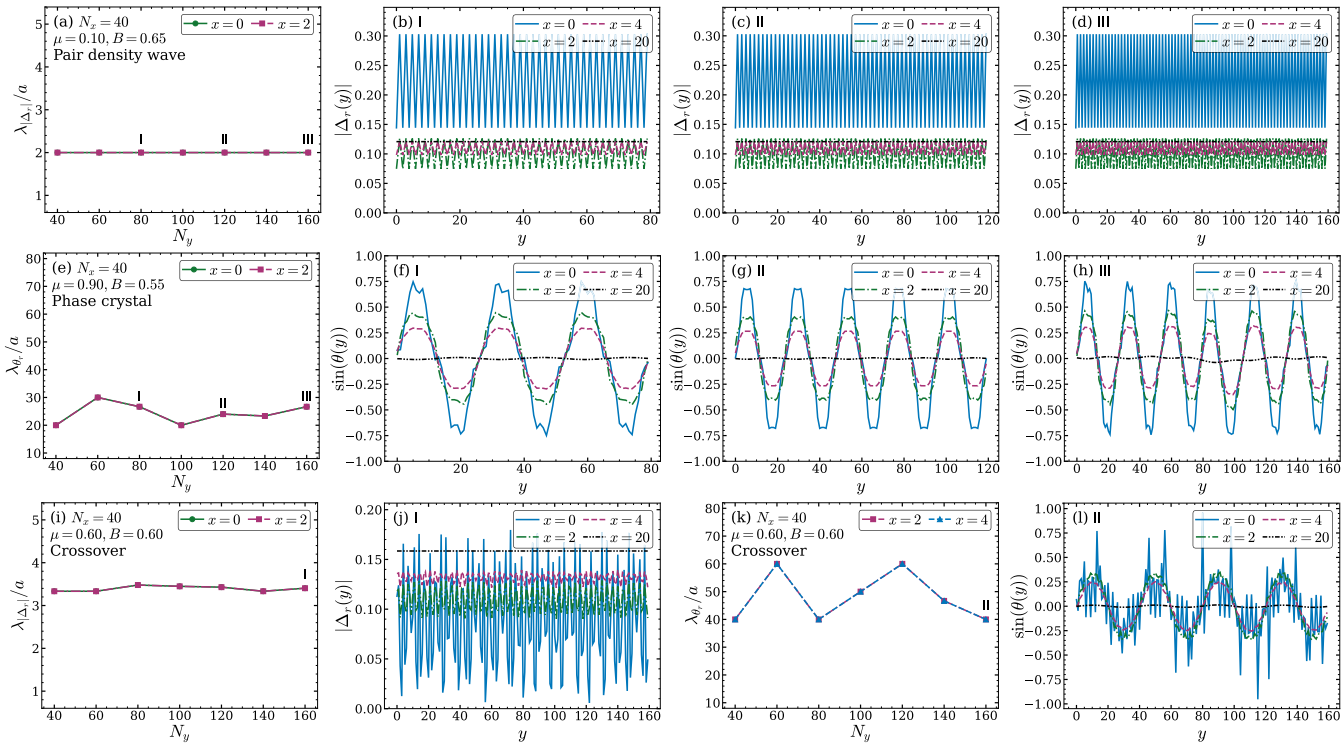


FIG. 9. (top row) (a)–(d) Pair density wave state, (middle row) (e)–(h) phase crystal state, and (bottom row) (i)–(l) a crossover state at zero temperature, corresponding to parameters $(\mu, B) = (0.10, 0.65)$, $(0.90, 0.55)$, and $(0.60, 0.60)$, respectively. Spatial wavelength of the (a) and (i) amplitude modulation and (e) and (k) phase modulations along the edge (y direction) as a function of N_y for fixed $N_x = 40$. (b)–(d), (f)–(h), and (j) and (l). Corresponding line plots of amplitude and phase modulations as a function of position y along the edge for several fixed values of x, with $x = 0$ being the edge and $x = 20$ representing the bulk.

calculations, fixing $N_x = 40$ and varying N_y from 40 to 160. This is to verify that the results are not an artifact of a finite N_y. For this data, we compute the dominant frequency component $q_{\max}$, corresponding to the maximum intensity in the Fourier power spectrum, for both the amplitude and the phase along the edge at several fixed values of x for the converged solution with the lowest free energy. From this, we extract the spatial wavelengths $\lambda = 1/q_{\max}$ of the amplitude ($\lambda_{|\Delta_r|}$) and phase (λ_{θ_r}) modulations along the edge (y direction).

The pair density wave, here extracted at $(\mu, B) = (0.10, 0.65)$, has a modulation period $\lambda_{|\Delta_r|} = 2a$, i.e., a bond-wave order, for all different values of N_y, as shown in Fig. 9(a). Line plots at specific x values, ranging from the edge $x = 0$ to the interior $x = 20$, of the amplitude modulation at points I–III in Fig. 9(a) are shown in Figs. 9(b)–9(d). Similarly, Figs. 9(e)–9(h) present the phase modulation period and line plots of the phase crystal at $(\mu, B) = (0.90, 0.55)$. The phase crystal acquires a periodicity of $\lambda_{\theta_r} \sim 20a$–$30a$, showing only small finite-size corrections for varying N_y. Finally, as shown in Figs. 9(i) and 9(k), the crossover state at $(\mu, B) = (0.60, 0.60)$ inherits features from both phases, exhibiting $\lambda_{|\Delta_r|} \approx 3.4a$, and $\lambda_{\theta_r} \sim 40a$–$60a$ across N_y. Figures 9(j) and 9(l) further show the corresponding line plots for amplitude and phase modulations at $N_y = 140$. This establishes that a finite N_y has a minimal effect on the spatial modulations. We note that the small finite-size corrections we find in the phase modulations stem from incommensurability effects, as the phase crystal and crossover states need to accommodate pairs of counterflowing current loops along the edge.

[1] A. A. Abrikosov, On the magnetic properties of superconductors of the second group, Sov. Phys. JETP **5**, 1174 (1957).

[2] P. Fulde and R. A. Ferrell, Superconductivity in a strong spin-exchange field, Phys. Rev. **135**, A550 (1964).

[3] A. I. Larkin and Y. N. Ovchinnikov, Nonuniform state of superconductors, Zh. Eksp. Teor. Fiz. **47**, 1136 (1964) [Sov. Phys. JETP **20**, 762 (1965)].

[4] A. Himeda, T. Kato, and M. Ogata, Stripe states with spatially oscillating d-wave superconductivity in the two-dimensional t-t'-J model, Phys. Rev. Lett. **88**, 117001 (2002).

[5] E. Berg, E. Fradkin, E.-A. Kim, S. A. Kivelson, V. Oganesyan, J. M. Tranquada, and S. C. Zhang, Dynamical layer decoupling in a stripe-ordered high-T_c superconductor, Phys. Rev. Lett. **99**, 127003 (2007).

[6] D. Agterberg and H. Tsunetsugu, Dislocations and vortices in pair-density-wave superconductors, Nat. Phys. **4**, 639 (2008).

[7] E. Berg, E. Fradkin, and S. A. Kivelson, Theory of the striped superconductor, Phys. Rev. B **79**, 064515 (2009).

[8] M. Barkman, A. Samoilenka, and E. Babaev, Surface pair-density-wave superconducting and superfluid states, Phys. Rev. Lett. **122**, 165302 (2019).

[9] A. B. Vorontsov, Andreev bound states in superconducting films and confined superfluid ^{3}He, Philos. Trans. R. Soc. A **376**, 20150144 (2018).

[10] C.-R. Hu, Midgap surface states as a novel signature for d^2_{xa}-x^2_b-wave superconductivity, Phys. Rev. Lett. **72**, 1526 (1994).

[11] M. Matsumoto and H. Shiba, Coexistence of different symmetry order parameters near a surface in d-wave superconductors III, J. Phys. Soc. Jpn. **65**, 2194 (1996).

[12] M. Fogelström, D. Rainer, and J. A. Sauls, Tunneling into current-carrying surface states of high-T_c superconductors, Phys. Rev. Lett. **79**, 281 (1997).

[13] M. Sigrist, Time-reversal symmetry breaking states in high-temperature superconductors, Prog. Theor. Phys. **99**, 899 (1998).

[14] Y. Nagai, Y. Ota, and K. Tanaka, Time-reversal symmetry breaking and gapped surface states due to spontaneous emergence of new order in d-wave nanoislands, Phys. Rev. B **96**, 060503 (2017).

[15] S. Matsubara and H. Kontani, Emergence of $d \pm ip$-wave superconducting state at the edge of d-wave superconductors mediated by ferromagnetic fluctuations driven by Andreev bound states, Phys. Rev. B **101**, 235103 (2020).

[16] T. Löfwander, V. S. Shumeiko, and G. Wendin, Time-reversal symmetry breaking at Josephson tunnel junctions of purely d-wave superconductors, Phys. Rev. B **62**, R14653(R) (2000).

[17] C. Honerkamp, K. Wakabayashi, and M. Sigrist, Instabilities at [110] surfaces of $d_{x^2-y^2}$ superconductors, Europhys. Lett. **50**, 368 (2000).

[18] A. C. Potter and P. A. Lee, Edge ferromagnetism from Majorana flat bands: Application to split tunneling-conductance peaks in high-T_c cuprate superconductors, Phys. Rev. Lett. **112**, 117002 (2014).

[19] A. M. Black-Schaffer, D. S. Golubev, T. Bauch, F. Lombardi, and M. Fogelström, Model evidence of a superconducting state with a full energy gap in small cuprate islands, Phys. Rev. Lett. **110**, 197001 (2013).

[20] P. Holmvall, A. B. Vorontsov, M. Fogelström, and T. Löfwander, Broken translational symmetry at edges of high-temperature superconductors, Nat. Commun. **9**, 2190 (2018).

[21] P. Holmvall, A. B. Vorontsov, M. Fogelström, and T. Löfwander, Spontaneous symmetry breaking at surfaces of d-wave superconductors: Influence of geometry and surface ruggedness, Phys. Rev. B **99**, 184511 (2019).

[22] M. Håkansson, T. Löfwander, and M. Fogelström, Spontaneously broken time-reversal symmetry in high-temperature superconductors, Nat. Phys. **11**, 755 (2015).

[23] P. Holmvall, M. Fogelström, T. Löfwander, and A. B. Vorontsov, Phase crystals, Phys. Rev. Res. **2**, 013104 (2020).

[24] N. W. Wennerdal, A. Ask, P. Holmvall, T. Löfwander, and M. Fogelström, Breaking time-reversal and translational symmetry at edges of d-wave superconductors: Microscopic theory and comparison with quasiclassical theory, Phys. Rev. Res. **2**, 043198 (2020).

[25] K. M. Seja, N. Wall-Wennerdal, T. Löfwander, and M. Fogelström, Spontaneous splitting of d-wave surface states: Competition between circulating currents and edge magnetization, Phys. Rev. B **110**, 064502 (2024).

[26] A. Joki, M. Fogelström, and T. Löfwander, Strengthened correlations near [110] edges of d-wave superconductors in the t-J model with the Gutzwiller approximation, Phys. Rev. B **113**, 024508 (2026).

[27] G. Sato, Y. Nagato, and S. Higashitani, Revisiting the surface density of states of midgap Andreev edge states, arXiv:2605.02423.

[28] M. Sigrist, K. Kuboki, P. A. Lee, A. J. Millis, and T. M. Rice, Influence of twin boundaries on Josephson junctions between high-temperature and conventional superconductors, Phys. Rev. B **53**, 2835 (1996).

[29] Y. Tanuma, Y. Tanaka, M. Ogata, and S. Kashiwaya, Theory of local density of states of dx^2-y^2-wave superconducting state near the surfaces of the t-J model, J. Phys. Soc. Jpn. **67**, 1118 (1998).

[30] S. Higashitani, Mechanism of paramagnetic Meissner effect in high-temperature superconductors, J. Phys. Soc. Jpn. **66**, 2556 (1997).

[31] A. L. Fauchère, W. Belzig, and G. Blatter, Paramagnetic instability at normal-metal–superconductor interfaces, Phys. Rev. Lett. **82**, 3336 (1999).

[32] Y. S. Barash, M. S. Kalenkov, and J. Kurkijärvi, Low-temperature magnetic penetration depth in d-wave superconductors: Zero-energy bound state and impurity effects, Phys. Rev. B **62**, 6665 (2000).

[33] A. B. Vorontsov, Broken translational and time-reversal symmetry in unconventional superconducting films, Phys. Rev. Lett. **102**, 177001 (2009).

[34] S.-I. Suzuki and Y. Asano, Paramagnetic instability of small topological superconductors, Phys. Rev. B **89**, 184508 (2014).

[35] D. Chakraborty, T. Löfwander, M. Fogelström, and A. M. Black-Schaffer, Disorder-robust phase crystal in high-temperature superconductors stabilized by strong correlations, npj Quantum Mater. **7**, 44 (2022).

[36] P. M. Bonetti, D. Chakraborty, X. Wu, and A. P. Schnyder, Interaction-driven first-order and higher-order topological superconductivity, Phys. Rev. B **109**, L180509 (2024).

[37] K. M. Seja, N. Wall-Wennerdal, T. Löfwander, A. M. Black-Schaffer, M. Fogelström, and P. Holmvall, Impurity strength–temperature phase diagram with phase crystals and competing time-reversal symmetry breaking states in nodal d-wave superconductors, Phys. Rev. B **111**, 094513 (2025).

[38] M. Covington, M. Aprili, E. Paraoanu, L. H. Greene, F. Xu, J. Zhu, and C. A. Mirkin, Observation of surface-induced broken time-reversal symmetry in $YBa_2Cu_3O_7$ tunnel junctions, Phys. Rev. Lett. **79**, 277 (1997).

[39] L. Alff, H. Takashima, S. Kashiwaya, N. Terada, H. Ihara, Y. Tanaka, M. Koyanagi, and K. Kajimura, Spatially continuous zero-bias conductance peak on (110) $YBa_2Cu_3O_{7-\delta}$ surfaces, Phys. Rev. B **55**, R14757(R) (1997).

[40] J. Y. T. Wei, N.-C. Yeh, D. F. Garrigus, and M. Strasik, Directional tunneling and Andreev reflection on $YBa_2Cu_3O_{7-\delta}$ single crystals: Predominance of d-wave pairing symmetry verified with the generalized Blonder, Tinkham, and Klapwijk theory, Phys. Rev. Lett. **81**, 2542 (1998).

[41] Y. Dagan and G. Deutscher, Doping and magnetic field dependence of in-plane tunneling into $YBa_2Cu_3O_{7-x}$: Possible evidence for the existence of a quantum critical point, Phys. Rev. Lett. **87**, 177004 (2001).

[42] W. K. Neils and D. J. Van Harlingen, Experimental test for subdominant superconducting phases with complex order parameters in cuprate grain boundary junctions, Phys. Rev. Lett. **88**, 047001 (2002).

[43] Y. Li, D. Wang, and C. Wu, Spontaneous breaking of time-reversal symmetry in the orbital channel for the boundary Majorana flat bands, New J. Phys. **15**, 085002 (2013).

[44] R. Wakatsuki, M. Ezawa, and N. Nagaosa, Majorana fermions and multiple topological phase transition in Kitaev ladder topological superconductors, Phys. Rev. B **89**, 174514 (2014).

[45] T. Mizushima and M. Sato, Topological phases of quasi-one-dimensional fermionic atoms with a synthetic gauge field, New J. Phys. **15**, 075010 (2013).

[46] D. Wang, Z. Huang, and C. Wu, Fate and remnants of Majorana zero modes in a quantum wire array, Phys. Rev. B **89**, 174510 (2014).

[47] C. Qu, M. Gong, Y. Xu, S. Tewari, and C. Zhang, Majorana fermions in quasi-one-dimensional and higher-dimensional ultracold optical lattices, Phys. Rev. A **92**, 023621 (2015).

[48] H. Hu, F. Zhang, and C. Zhang, Majorana doublets, flat bands, and Dirac nodes in *s*-wave superfluids, Phys. Rev. Lett. **121**, 185302 (2018).

[49] References [6,7] formally define a pair density wave as a spatially modulating superconducting state with a vanishing average. The nonuniform superconducting state found in this work is an induced pair density wave localized near the edge within a uniform bulk order parameter. Therefore, its spatial average does not vanish. However, we still refer to this state as a pair density wave.

[50] T.-P. Choy, J. M. Edge, A. R. Akhmerov, and C. W. J. Beenakker, Majorana fermions emerging from magnetic nanoparticles on a superconductor without spin-orbit coupling, Phys. Rev. B **84**, 195442 (2011).

[51] I. Martin and A. F. Morpurgo, Majorana fermions in superconducting helical magnets, Phys. Rev. B **85**, 144505 (2012).

[52] F. Pientka, L. I. Glazman, and F. von Oppen, Topological superconducting phase in helical Shiba chains, Phys. Rev. B **88**, 155420 (2013).

[53] Y. Kim, M. Cheng, B. Bauer, R. M. Lutchyn, and S. Das Sarma, Helical order in one-dimensional magnetic atom chains and possible emergence of Majorana bound states, Phys. Rev. B **90**, 060401 (2014).

[54] M. Schecter, K. Flensberg, M. H. Christensen, B. M. Andersen, and J. Paaske, Self-organized topological superconductivity in a Yu-Shiba-Rusinov chain, Phys. Rev. B **93**, 140503 (2016).

[55] S. Nadj-Perge, I. K. Drozdov, B. A. Bernevig, and A. Yazdani, Proposal for realizing Majorana fermions in chains of magnetic atoms on a superconductor, Phys. Rev. B **88**, 020407 (2013).

[56] K. Pöyhönen, A. Westström, J. Röntynen, and T. Ojanen, Majorana states in helical Shiba chains and ladders, Phys. Rev. B **89**, 115109 (2014).

[57] N. Sedlmayr, J. M. Aguiar-Hualde, and C. Bena, Flat Majorana bands in two-dimensional lattices with inhomogeneous magnetic fields: Topology and stability, Phys. Rev. B **91**, 115415 (2015).

[58] A. V. Balatsky, I. Vekhter, and J.-X. Zhu, Impurity-induced states in conventional and unconventional superconductors, Rev. Mod. Phys. **78**, 373 (2006).

[59] J. Röntynen and T. Ojanen, Topological superconductivity and high Chern numbers in 2D ferromagnetic Shiba lattices, Phys. Rev. Lett. **114**, 236803 (2015).

[60] J. Li, T. Neupert, Z. Wang, A. H. MacDonald, A. Yazdani, and B. Andrei Bernevig, Two-dimensional chiral topological superconductivity in Shiba lattices, Nat. Commun. **7**, 12297 (2016).

[61] L. Schneider, P. Beck, T. Posske, D. Crawford, E. Mascot, S. Rachel, R. Wiesendanger, and J. Wiebe, Topological Shiba bands in artificial spin chains on superconductors, Nat. Phys. **17**, 943 (2021).

[62] P. Chatterjee, S. Banik, S. Bera, A. K. Ghosh, S. Pradhan, A. Saha, and A. K. Nandy, Topological superconductivity by engineering noncollinear magnetism in magnet/superconductor heterostructures: A realistic prescription for the two-dimensional Kitaev model, Phys. Rev. B **109**, L121301 (2024).

[63] N. Sedlmayr, M. Guigou, P. Simon, and C. Bena, Majoranas with and without a 'character': Hybridization, braiding and chiral Majorana number, J. Phys.: Condens. Matter **27**, 455601 (2015).

[64] B. W. Heinrich, J. I. Pascual, and K. J. Franke, Single magnetic adsorbates on *s*-wave superconductors, Prog. Surf. Sci. **93**, 1 (2018).

[65] S.-H. Ji, T. Zhang, Y.-S. Fu, X. Chen, X.-C. Ma, J. Li, W.-H. Duan, J.-F. Jia, and Q.-K. Xue, High-resolution scanning tunneling spectroscopy of magnetic impurity induced bound states in the superconducting gap of Pb thin films, Phys. Rev. Lett. **100**, 226801 (2008).

[66] M. Ruby, F. Pientka, Y. Peng, F. von Oppen, B. W. Heinrich, and K. J. Franke, End states and subgap structure in proximity-coupled chains of magnetic adatoms, Phys. Rev. Lett. **115**, 197204 (2015).

[67] A. Kamlapure, L. Cornils, J. Wiebe, and R. Wiesendanger, Engineering the spin couplings in atomically crafted spin chains on an elemental superconductor, Nat. Commun. **9**, 3253 (2018).

[68] K. Yang, W. Paul, S.-H. Phark, P. Willke, Y. Bae, T. Choi, T. Esat, A. Ardavan, A. J. Heinrich, and C. P. Lutz, Coherent spin manipulation of individual atoms on a surface, Science **366**, 509 (2019).

[69] C. Mier, J. Hwang, J. Kim, Y. Bae, F. Nabeshima, Y. Imai, A. Maeda, N. Lorente, A. Heinrich, and D.-J. Choi, Atomic manipulation of in-gap states in the β-Bi_2Pd superconductor, Phys. Rev. B **104**, 045406 (2021).

[70] S. Rachel and R. Wiesendanger, Majorana quasiparticles in atomic spin chains on superconductors, Phys. Rep. **1099**, 1 (2025).

[71] S. Nadj-Perge, I. K. Drozdov, J. Li, H. Chen, S. Jeon, J. Seo, A. H. MacDonald, B. A. Bernevig, and A. Yazdani, Observation of Majorana fermions in ferromagnetic atomic chains on a superconductor, Science **346**, 602 (2014).

[72] H. Kim, A. Palacio-Morales, T. Posske, L. Rózsa, K. Palotás, L. Szunyogh, M. Thorwart, and R. Wiesendanger, Toward tailoring Majorana bound states in artificially constructed magnetic atom chains on elemental superconductors, Sci. Adv. **4**, eaar5251 (2018).

[73] L. Schneider, S. Brinker, M. Steinbrecher, J. Hermenau, T. Posske, M. dos Santos Dias, S. Lounis, R. Wiesendanger, and J. Wiebe, Controlling in-gap end states by linking nonmagnetic atoms and artificially-constructed spin chains on superconductors, Nat. Commun. **11**, 4707 (2020).

[74] L. Schneider, P. Beck, J. Neuhaus-Steinmetz, L. Rózsa, T. Posske, J. Wiebe, and R. Wiesendanger, Precursors of Majorana modes and their length-dependent energy oscillations probed at both ends of atomic Shiba chains, Nat. Nanotechnol. **17**, 384 (2022).

[75] D. Crawford, E. Mascot, M. Shimizu, P. Beck, J. Wiebe, R. Wiesendanger, H. O. Jeschke, D. K. Morr, and S. Rachel, Majorana modes with side features in magnet-superconductor hybrid systems, npj Quantum Mater. **7**, 117 (2022).

[76] M. O. Soldini, F. Küster, G. Wagner, S. Das, A. Aldarawsheh, R. Thomale, S. Lounis, S. S. P. Parkin, P. Sessi, and T. Neupert, Two-dimensional Shiba lattices as a possible platform for crystalline topological superconductivity, Nat. Phys. **19**, 1848 (2023).

[77] R. Brüning, J. Bedow, R. L. Conte, K. von Bergmann, D. K. Morr, and R. Wiesendanger, The noncollinear path to two-dimensional topological superconductivity, ACS Nano **19**, 36215 (2025).

[78] J.-X. Zhu, *Bogoliubov–de Gennes Method and Its Applications*, Lecture Notes in Physics, Vol. 924 (Springer International Publishing, Cham, 2016).

[79] L. Rózsa, L. Udvardi, L. Szunyogh, and I. A. Szabó, Magnetic phase diagram of an Fe monolayer on W(110) and Ta(110) surfaces based on *ab initio* calculations, Phys. Rev. B **91**, 144424 (2015).

[80] A. Altland and M. R. Zirnbauer, Nonstandard symmetry classes in mesoscopic normal-superconducting hybrid structures, Phys. Rev. B **55**, 1142 (1997).

[81] A. P. Schnyder, S. Ryu, A. Furusaki, and A. W. W. Ludwig, Classification of topological insulators and superconductors in three spatial dimensions, Phys. Rev. B **78**, 195125 (2008).

[82] L. Fu, C. L. Kane, and E. J. Mele, Topological insulators in three dimensions, Phys. Rev. Lett. **98**, 106803 (2007).

[83] J. E. Moore and L. Balents, Topological invariants of time-reversal-invariant band structures, Phys. Rev. B **75**, 121306 (2007).

[84] R. Roy, Topological phases and the quantum spin Hall effect in three dimensions, Phys. Rev. B **79**, 195322 (2009).

[85] S. Ryu and Y. Hatsugai, Topological origin of zero-energy edge states in particle-hole symmetric systems, Phys. Rev. Lett. **89**, 077002 (2002).

[86] S. Ryu, A. P. Schnyder, A. Furusaki, and A. W. W. Ludwig, Topological insulators and superconductors: Tenfold way and dimensional hierarchy, New J. Phys. **12**, 065010 (2010).

[87] X. G. Wen and A. Zee, Winding number, family index theorem, and electron hopping in a magnetic field, Nucl. Phys. B **316**, 641 (1989).

[88] M. Sato, Y. Tanaka, K. Yada, and T. Yokoyama, Topology of Andreev bound states with flat dispersion, Phys. Rev. B **83**, 224511 (2011).

[89] Y. Niu, S. B. Chung, C.-H. Hsu, I. Mandal, S. Raghu, and S. Chakravarty, Majorana zero modes in a quantum Ising chain with longer-ranged interactions, Phys. Rev. B **85**, 035110 (2012).

[90] S. Tewari and J. D. Sau, Topological invariants for spin-orbit coupled superconductor nanowires, Phys. Rev. Lett. **109**, 150408 (2012).

[91] J. Barzilai and J. M. Borwein, Two-point step size gradient methods, IMA J. Numer. Anal. **8**, 141 (1988).

[92] P. Holmvall, N. Wall Wennerdal, M. Håkansson, P. Stadler, O. Shevtsov, T. Löfwander, and M. Fogelström, SuperConga: An open-source framework for mesoscopic superconductivity, Appl. Phys. Rev. **10**, 011317 (2023).

[93] I. Kosztin, Š. Kos, M. Stone, and A. J. Leggett, Free energy of an inhomogeneous superconductor: A wave-function approach, Phys. Rev. B **58**, 9365 (1998).

[94] J. D. Sau and S. Tewari, Topologically protected surface Majorana arcs and bulk Weyl fermions in ferromagnetic superconductors, Phys. Rev. B **86**, 104509 (2012).

[95] N. F. Q. Yuan, C. L. M. Wong, and K. T. Law, Probing majorana flat bands in nodal $d_{x^2-y^2}$-wave superconductors with Rashba spin-orbit coupling, Physica E **55**, 30 (2014).

[96] Immediately after the system enters the topologically nontrivial phase, specifically at $B = 0.45$ and 0.50, we need to halve the bounds on the mean RMS phase deviation $\delta\theta$ for consistent behavior. This reduction primarily accounts for the lower number of Majorana states in this parameter range than in the rest of the phase diagram, leading to not needing as large phase variations to shift states away from zero energy.

[97] X. Chen, Essay: Generalized Landau paradigm for quantum phases and phase transitions, Phys. Rev. Lett. **135**, 250001 (2025).

[98] S. Varada, A. Kobiałka, A. Bhattacharya, P. Holmvall, and A. M. Black-Schaffer, Data and code for "Nonuniform superconducting states from Majorana flat bands" [Dataset], Zenodo (2026), doi: 10.5281/zenodo.19855861.